

ALMA MATER STUDIORUM · UNIVERSITY OF BOLOGNA

School of Science
Department of Physics and Astronomy
Master Degree in Physics

Spectral properties of resonant Bose-Fermi mixtures

Supervisor:
Prof. Pierbiagio Pieri

Submitted by:
Pietro Micaletti

Academic Year 2022/2023

Magna vis est in virtutibus; eas
excita, si forte dormiunt.

M. T. Cicero

There is great strength in the
virtues; wake them up, if by chance
they sleep.

M. T. Cicero

To my family.

Abstract

The object of study of the present work are Bose-Fermi mixtures in three dimensions at zero temperature. The system is characterized by a great tunability of physical parameters that is achieved by means of a Fano-Feshbach resonance. As a result, there are mainly two regimes: we move from a situation in which bosons and fermions are weakly interacting to a context in which bosons are coupled to fermions so as to form molecules that are composite fermions, as the coupling between the two types of particles is increased. In the former case, we can describe the mixture as a weakly attractive Bose-Fermi one, while in the latter the same is described in terms of molecules and excess atoms or particles which are unpaired. The main aim of the thesis is to analyze the spectral weight functions which represent the single-particle excitation spectra of the system and are relevant to recent radio-frequency spectroscopy experiments of the system. In order to pursue this objective, diagrammatic methods are used. The formalism is developed within the T-matrix approach: it consists of an approximate calculation which selects exclusively the class of Feynman's diagrams that collects all possible repeated boson-fermion interaction.

Contents

Introduction	ix
1 Ultracold Bose-Fermi mixtures	1
1.1 Short digression on ultracold gases	1
1.2 Fano-Feshbach resonances	3
1.3 Theoretical and experimental works	5
1.4 Latest experiments	12
2 A theoretical approach to Bose-Fermi mixtures	15
2.1 The model Hamiltonian	15
2.2 T -matrix approach	17
2.3 Fermionic and bosonic self-energies	21
2.4 Green's functions, momentum distributions and density	23
2.5 Analytic continuation and poles of the retarded T -matrix	25
2.6 Poles of the retarded Green's function and quasi-particle residue	29
2.7 Manipulation of the integrals involved in the fermionic and bosonic retarded self-energies	30
2.8 Momentum distribution functions	35
3 Building the program	37
3.1 Adimensionalization of physical quantities	37
3.2 The code	39
3.2.1 T -matrices, poles and dispersions	39
3.2.2 Retarded self-energies, spectral weight functions and numerical checks	42

4	Numerical results and analysis	45
4.1	Retarded T -matrix	45
4.1.1	Retarded Γ -matrix	45
4.1.2	Retarded T -matrix T^R	49
4.2	Fermi momentum $P_{\Gamma}^0, P_{T_1}^0, P_{T_2}^0$ and dispersions	51
4.3	Spectral weight functions	56
4.4	Numerical checks	60
4.4.1	Sum rule	60
4.4.2	Fermionic momentum distribution function	60
4.4.3	Quasi-particle residue	62
5	Outlooks and concluding remarks	63
5.1	Future perspectives	63
5.2	Concluding remarks	65
A	Quasi-particle theory	67
B	Bisection method	71
C	Gauss-Legendre integration	73
	Bibliography	75
	Acknowledgements	81

Introduction

Ultracold gases are one of the best physical platforms where new phases of matter can emerge (e.g. superfluidity) which are in turn at the basis of in the realization of new technological and experimental innovations with a significant impact also on everyday life. They are regarded as quantum simulators because, thanks to their great flexibility and broad tunability of the physical parameters, allow us to study and explore the behaviour of quantum matter in a controlled way, making a better understanding of several phenomena, ranging from nuclear many-body theory to high T_c superconductors, possible. Bose-Fermi mixtures are quantum simulators *par excellence* being systems in which, in the presence of a Fano-Feshbach resonance, the strength of the interactions between its constituents, i.e. bosons and fermions, can be tuned at will by acting, typically with an external magnetic field near the resonance, on coupling strength parameter. In this thesis we address the study of the competition between the coupling, which is responsible for the formation of composite fermions (i.e. molecules composed by one boson and one fermion), and the condensation of the bosons in their ground state. Clearly, as the former increases, the latter is reduced and vice versa. A system characterized by a higher concentration of fermions rather than bosons behaves in a complete different way than a system in which the role of predominance is switched between the two species, i.e. bosons are more than fermions. This is because, in the first case, above a certain coupling strength, composite fermions - which are molecules composed by one fermion and one boson - will be subjected to a repulsive interaction towards the excess atoms/particles for the reason that the latter are fermions and, therefore, a sort of molecular Pauli exclusion principle holds: on one hand a fermion (which is composite), on the other another one, so they repel each other. In the second case instead, the aforementioned interaction will be attractive owing to the excess atoms/particles are now bosons; as a result, there is no trace of Pauli

exclusion principle. This different behaviour is reflected in the profiles of several physical quantities, e.g. chemical potentials, condensate density and so on. In order to describe the aforementioned processes it is important to set up a proper theoretical formalism; to this end we use Green's functions at zero temperature with Feynman's diagrams computed within the framework of T -matrix approximation: by doing so, we took into account all possible repeated boson-fermion interaction, modeled by a contact potential, obtaining in this way a ladder and this is the reason why we call these diagrams *ladder diagrams*. The main aim of this thesis is, starting from the T -matrix approximation in the condensed phase, the construction of the spectral weight functions. One of the strongest motivations that led us to focus on this topic are the experimental results obtained by a group of researches at the University of Innsbruck [20] with regard to the excitation spectrum - related to the spectral weight functions - of a system made of bosonic ^{41}K impurities immersed in a ^6Li Fermi sea. In particular, a new branch, called BEC branch because it has been observed in the partially condensed regime, has emerged in the spectrum (which shows no sign of the Fermi polaron, as in the case of the thermal cloud regime). Some hypotheses have been put forward to explain this unexpected behaviour, but the question deserves further investigations since a proper theoretical study in the condensed regime has not been carried out yet.

The present work, which involves analytical calculations as well as numerical ones, is structured in five Chapters. In the first one, we present the state of the art on ultracold gases and Bose-Fermi mixtures giving an insight on Fano-Feshbach resonances, the theoretical and experimental works, the techniques that are behind the realization of this type of systems as well as the more recent experiments.

In the second Chapter we begin by formally describing the physical system by means of the T -matrix approach and the corresponding fermionic and bosonic self-energies, which are used to get the dressed Green's functions via the Dyson's equation. Moreover, we introduce the concept of analytic continuation, which is crucial to obtain the spectral weight functions. In the second part of the Chapter,

in addition to dwelling on the quasi-particle residue and the momentum distribution functions, we focus on the poles of the retarded T -matrix and Green's function, which are useful in the subsequent manipulation of the integrals involved in the self-energies. This is a necessary step also for the purpose of implementing the numerical calculations whose in-depth analysis is the content of the third Chapter. Here, the building and the functioning of the numerical work are illustrated, starting from the adimensionalization of the equations and ending with the implementation of the calculation of the quasi-particle residue.

Chapter 4 is devoted to the presentation of the results obtained with the numerical calculations and their discussion: in particular, retracing the theoretical considerations made in Chapter 2, we show the behaviour of the retarded T -matrix as the coupling parameter is varied focusing on its poles and their dispersions too. The core of this Chapter is the analysis of the fermionic spectral weight function as a function of the momentum and frequency for given values of the coupling parameter. We conclude the Chapter by discussing some numerical checks, the fermionic momentum distribution function and its jumps whose height is described by the quasi-particle residue.

In the final Chapter we discuss some outlooks and perspectives.

In the Appendices one can find a very short discussion about the bisection method, which is used in the program for the determination of the poles, and the Gauss-Legendre integration that were implemented in our code, as well as a brief description of quasi-particle theory.

Chapter 1

Ultracold Bose-Fermi mixtures

In this first Chapter we briefly discuss the state of the art on ultracold Bose-Fermi mixtures (in three dimensions). Before doing that, we focus on ultracold gases in general and Fano-Feshbach resonances since they can be regarded as the building blocks of the systems that we aim to study.

1.1 Short digression on ultracold gases

When dealing with ultracold gases, there are some fundamental premises that must be made: first of all, three length scales rule these systems and are the thermal de Broglie wavelength $\lambda_T = \sqrt{2\pi\hbar/mk_B T}$ (where $\hbar = 6.62607015/2\pi \times 10^{-34} J \cdot s$ is the reduced Planck constant, m is the atomic mass, $k_B = 1.380649 \times 10^{-23} J/K$ is the Boltzmann constant and T is the temperature), which represents the size of the wave-packet associated to a particle, the range of the interaction r_0 and the average interparticle distance $l \approx n^{-d}$ (n is the particle density of a d -dimensional system). Secondly, these systems are characterized by low densities and temperatures: for instance, if we consider an atomic cloud made of Bose-Einstein condensate, typically its particle density is about $10^{13} - 10^{15} \text{ cm}^{-3}$ while the temperatures are approximately of the order of the microkelvin (μK). When the thermal de Broglie wavelength becomes comparable or larger than the average interparticle distance ($l \lesssim \lambda_T$), the Maxwell-Boltzmann statistics which reproduces the behaviour of classical particles is no longer suitable to describe the

system since quantum phenomena arise. In this quantum degeneracy regime, particles can all be described in terms of Bose-Einstein statistics, if they have integer spin, or Fermi-Dirac statistics, if they have half-integer spin. Particles that obey to the former statistics are called bosons, while in the latter case we are dealing with fermions.

As stated previously, the density of the system should be very low as well as the temperature - otherwise its almost exact description is doomed to failure - and this condition is satisfied whenever the range of the interaction is significantly smaller than the interparticle distance ($r_0 \ll l$). The latter is a necessary condition for the system to remain gas and not crystallize and leads to the description of the interactions by means of a contact potential. Since we aim to study a gas in a quantum regime, if $r_0 \ll l$, then, all the more reason, $r_0 \ll \lambda_T$; by requiring that, the scattering processes in which particles are constantly involved achieve the traits of universality since the corresponding problem does not depend on the characteristics of the interatomic potential anymore but rather on the features of the lowest angular momentum scattering length a . This regime is of great physical interest because striking quantum phenomena can occur, e.g. superfluidity or Bose-Einstein condensation.

In particular, Bose-Einstein condensates (BEC) were predicted theoretically in 1925 by Einstein [1] after the study of Bose regarding the photonic statistics [2]: the most interesting aspect was the existence of a new phase below a critical temperature in which a finite fraction of the bosons occupies the single-particle state with momentum equal to zero. The experimental realization of a BEC took place only in 1995 at the University of Colorado in the laboratories of Boulder with atoms of ^{87}Rb [3] and at Massachusetts Institute of Technology (MIT) with ^{23}Na [4]. The direct observation of ultracold gases has been made possible by mean of cooling techniques as well as trapping ones. As for the former, they consist of laser and evaporative cooling, while the latter are mainly divided into three categories: magnetic traps, optical traps and magneto-optical traps (known by their acronym as MOT).

Generally, there are two ways to tune the interactions between atoms: the first

method is to use different atomic species whilst in the second an applied magnetic field is varied to change the interaction whenever the species under consideration have a Fano-Feshbach resonance. In the latter case, it is possible to analyze the regime in which the scattering length is much larger than the average inter-particle distance, and the atomic cloud can be thought as a strongly-interacting many-body system. This is the focus of the following section.

1.2 Fano-Feshbach resonances

A Fano-Feshbach resonance is a multi-channel scattering phenomenon in which the elastic scattering in one channel can be varied significantly if in a second channel - that is closed - there is a low-energy bound state. When the energy of the latter is approached by the total energy of two scattering particles in an open channel a Fano-Feshbach resonance occurs. A second-order process modifies the scattering length of the problem and it works like this: in an open channel two particles can scatter to an intermediate state in a closed channel, which typically decays in two particles in one of the open channels. Due to this process, the scattering length is modified by terms of the type $a \propto \frac{1}{E_{op} - E_{cl}}$, where E_{cl} is the energy of a state in the closed channel, while E_{op} is the energy of a state in the open channels. As a result, the effect of the coupling between channels on the scattering length is particularly evident if the energies in the previous relation have similar values; these can be altered if one changes external parameters: the best candidate, as claimed before, is the external magnetic field B . With B_0 we denote the value of the field at which the threshold energy of the open channel reaches the bound-state energy in the closed channel. The magnetic moments in the two channels - open and closed ones - are in general different from each other so it is possible, by changing the value of B , to bring the bound-state energy closer to the threshold of the open channel. In the presence of a Fano-Feshbach resonance the behaviour of the scattering length is the following:

$$a = a_{bg} \left(1 - \frac{\Delta}{B - B_0} \right) \quad (1.1)$$

where a_{bg} is the background scattering length far from the resonance and Δ is the width parameter which depends on the different magnetic moments in the channels and on the coupling between them. If we are far away from the resonance, i.e. $|B - B_0| \ll 0$, then $a = a_{bg}$ since Δ is negligible compared to 1. If we assume $a_{bg} < 0$, as typically is, when we are close to the resonance the scattering length passes from negative values to the zero one (in this specific case $B - B_0 = \Delta$), then it increases and diverges for $B = B_0$ (leading to the so-called *unitarity limit* in the context of ultracold gases). Afterwards, it becomes small again. When the scattering length is small compared to the interparticle distance and positive, the binding energy of the bound states (which are made possible by the strong attractive interaction) is $\epsilon_0 = 1/2m_r a^2$ near the resonance (m_r is the reduced mass). This situation corresponds to the strongly-coupled Bose-Fermi mixture in the molecular limit, as we will see in the following. If this is not the case instead, there are no bound states and the system is weakly interacting (the scattering length takes negative values close to zero). Figure 1.1 summarizes the considerations made so far.

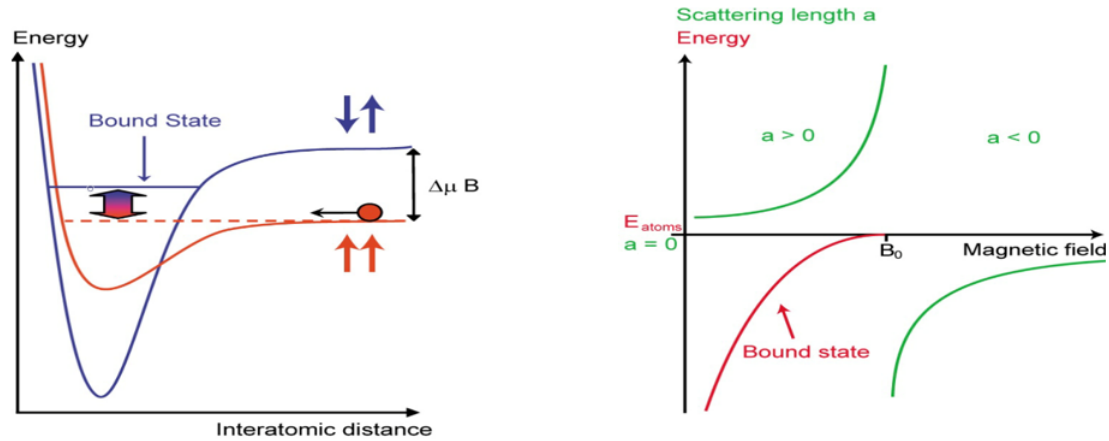


FIGURE 1.1: Left panel: formation of the Fano-Feshbach resonance. Two potential curves for two different channels - open and closed one - are depicted. Right panel: curves of the scattering length and of the binding energy as functions of the external magnetic field.

1.3 Theoretical and experimental works

The study, both theoretical and experimental, of Bose-Fermi mixtures has begun around the 2000s. As for the former, at first non-resonant mixtures have been taken into account within a mean-field approximation framework [5]. Here, the degenerate Fermi gas was induced to collapse by means of the interaction with a Bose-Einstein condensate. A further development in this description was provided by the introduction of beyond-mean-field corrections with regard to the ground-state properties [6]. Afterwards, Bose-Fermi mixtures have been explored in presence of a Fano-Feshbach resonance [7, 8]. There are two types of Fano-Feshbach resonances: one is called *broad* and the other *narrow*: in the first case, the scattering length and the average interparticle distance are bigger than the effective range of the potential, while in the second one this condition is no longer satisfied. However, for a narrow Fano-Feshbach resonance the Hamiltonian contains terms related to fermions, bosons and molecules formed in the closed channel; the latter contribution is not present if we are considering a broad Fano-Feshbach resonance. Bose-Fermi mixtures in lattices in the presence of a broad Fano-Feshbach resonance were the focus of the first works [9, 10, 11]. The continuum case has been taken into account with the modeling of the interaction between bosons and fermions as an attractive point-contact potential [12]. Quantum Monte Carlo approach has been recently considered when dealing with Bose-Fermi mixtures [13, 14] but this method is beyond the aim of the present thesis.

The practical realization of such mixtures has always been a difficult challenge for a number of reasons that we will discuss in a while. Recent works have shown that the possibility of tuning the interspecies scattering length via a Fano-Feshbach resonance is concrete. Moreover, some experiments, in which ^{23}Na - ^{40}K [15], ^{23}Na - ^6Li [16] and ^{87}Rb - ^{40}K [17] mixtures were employed, have succeed in the formation of ultracold molecules. In these cases, the standard molecular lifetime near the Fano-Feshbach resonance ranges from few milliseconds to several tens of milliseconds. In general, since in the region of intermediate coupling the system is characterized by heating processes and atom losses, experiments were severely limited in this regime. Such technical issues can be partially overcome by reducing the bosonic concentration so that the loss rate, being proportional to the fermionic density

times the square of the bosonic one, is significantly lowered. Regarding a possible mechanical collapse of the mixture, a sufficiently large boson-boson repulsion (i.e. above a certain threshold) should prevent it [18]. Bose-Fermi mixtures have also been studied and realized in two dimensions since the intermediate regime of the boson-fermion pairing can be better examined in a 2D-geometry confinement. An independent tuning of the boson-fermion and boson-boson interactions, in such a way that the boson-fermion attraction is swept across the entire Fano-Feshbach resonance and the necessary boson-boson repulsion is guaranteed, can be nowadays achieved if a confinement-induced resonance as well as a Fano-Feshbach one are applied simultaneously to the system [19].

Moving to days closer to us, a group of researchers at the University of Innsbruck has recently published a scientific report [20] in which they focused on a system made of ^{41}K and ^6Li atoms; in particular, the bosonic ^{41}K impurities are immersed in a Fermi sea of ultracold ^6Li atoms so that the system is highly imbalanced. As usual, interspecies interactions are largely tunable via Fano-Feshbach resonance. Radio-frequency injection spectroscopy is used to transfer atoms from a noninteracting spin state $|K|2\rangle$ into a state $|K|1\rangle$ which interacts with the fermionic medium. Three different impurity regimes have been taken into account (see Figure 1.2): in the first one, that is the case of a single impurity, the K atom turns out to be dressed by particle-hole excitation of the Fermi sea; this leads to local density modulations in the medium and to the formation of the Fermi polaron. In the single-impurity limit the quantum statistics of the minority species (i.e. bosons in the present case) is irrelevant for the behaviour of the ensemble. The experimental observations that were conducted in this regime have shown great agreement with the theoretical predictions based on Landau's quasiparticle theory. If more K atoms are added to the system, then polaron-polaron interactions are introduced: as a consequence, we assist at the spatial overlap of the density modulations around the impurities; this implies an effective interaction between the quasiparticles which is mediated by the fermions and is attractive owing to the bosonic nature of the ^{41}K atoms [21, 22]. However, experimental observations in this regime are quite limited due to technical issues [23]. The last scenario is the high-density regime, in which the impurities form a Bose-Einstein condensate

(BEC); typically, its density is significantly larger than that of the Fermi sea; therefore, the bosonic and the fermionic species interchange their roles and locally the ${}^6\text{Li}$ atoms can be seen as impurities in the K-BEC. Now the ensemble is described in terms of Bose polarons [24] and not anymore Fermi ones. As a result, since the density of the bosonic species can be varied from a thermal cloud to a BEC, it is possible to realize the transition from Fermi polarons to Bose polarons. Note that in the names *Fermi* or *Bose* polarons, the statistics refer to the medium in which the impurities (minority species) are embedded.

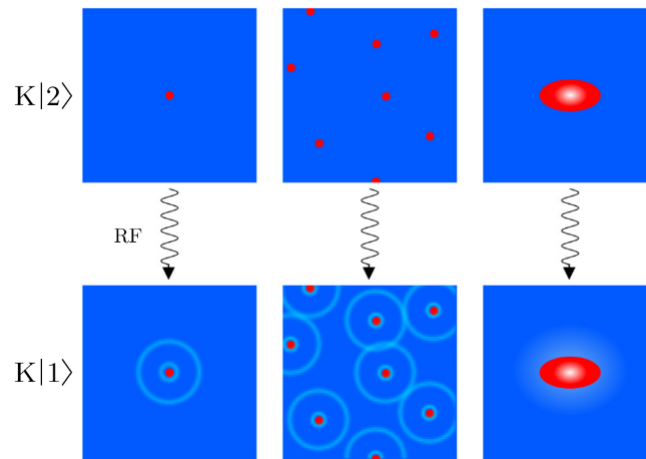


FIGURE 1.2: Fermi-Bose mixture in three different regimes, illustrated by the three columns. From left to right (the bosonic density is increased): single impurity regime, high density regime, mixed phase containing a large BEC component. The upper row shows the noninteracting impurities that is immersed on a Fermi sea, while the lower row illustrates the interacting ones [Figure reproduced from 20].

The focus is on the spectral response of the ${}^{41}\text{K}$ bosonic sample immersed in a ${}^6\text{Li}$ Fermi sea (see Figure 1.3). The spectra are a function of the coupling parameter and the dimensionless radio-frequency detuning $h\Delta\nu/\epsilon_f$, where $\Delta\nu = \nu_0 - \nu$ is the difference between the resonance frequency where the maximum transfer

from the noninteracting state $K|2\rangle$ to the interacting one $K|1\rangle$ occurs and the frequency effectively applied and ϵ_F is the Fermi energy. In the thermal cloud regime a typical polaron spectrum can be observed and it has the characteristic repulsive and attractive branch exhibiting a positive and negative energy shift, respectively. In this case, there is a good agreement with the theoretical predictions for the single-impurity framework. In the partially condensed regime instead, a new branch, called BEC branch, emerges in the spectrum, which shows no sign of the polaron anymore. There is a small positive shift in energy over a large range of interactions and a possible explanation for this could lie in an interchange of the role of the two atomic species: now the BEC could represent the environment, while the Fermi sea the impurities. This scenario, described by the Bose polaron (and no longer the Fermi one), suggests that these two may appear as different branches of one spectrum. Anyway, the question, still being debated, needs further investigations since a proper theoretical study in this regime has not been carried out yet.

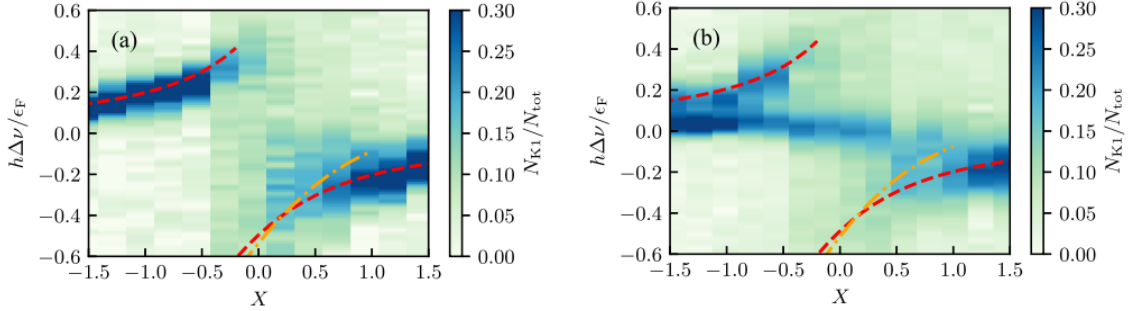


FIGURE 1.3: The first panel illustrates the excitation spectrum in the thermal cloud regime, while the second one refers to the partially condensed one. The color map shows the transferred fraction of atoms from $K|2\rangle$ to $K|1\rangle$. Dashed lines stand for theoretical predictions [Figure reproduced from 20].

All in all, in this experiment the existence of a transition from Fermi polarons to molecules has been established for impurities in a Fermi sea but there have been other works in which Bose polarons were observed in the limit of fermionic

impurities in a bosonic bath [25, 26].

Generally speaking, however, it was not clear in which terms the transition from atoms to molecules proceeds when the impurities are degenerate, especially when fermions and bosons, whose densities are comparable, dress each other respectively and alter their mutual behaviour in a dramatic way. The regime of matched particle density is particularly promising when it comes to the association of heteronuclear molecules at high phase space density. This type of study is of interest since it has several applications ranging from quantum chemistry to dipolar quantum-many body systems, but the achievement of such a regime is technically difficult in double-degenerate mixtures owing to the enhanced density of the bosonic condensate: the latter, in fact, is responsible for fast interspecies loss that, acting as a bottleneck, does not allow to reach quantum degeneracy in heteronuclear molecules and makes the investigation of strongly correlated Bose-Fermi mixtures much harder. These problems have been partially overcome by a team of researchers between Garching and Munchen in Germany. In their recent experimental work [27], they observed a transition from a polaronic condensate to a degenerate Fermi gas of heteronuclear molecules, more specifically a quantum phase transition - driven by strong boson-fermion interactions - from a polaronic phase to a molecular one in a density-matched degenerate Bose-Fermi mixture. In particular, they were able to produce a double-degenerate mixture of ^{23}Na and ^{40}K with matched density by means of a new species-dependent density-decompression technique of atomic clouds capable of mitigating atomic loss. The weakly interacting mixture is the starting point as usual; then, as interactions become stronger, the bosonic condensate is dressed polaronically. The interaction strength, tuned in a continuous way, causes the depletion of the polaronic condensate; therefore, a transition into a phase of quantum-degenerate fermionic molecules occurs. At this stage, by driving through the phase transition, a quantum-degenerate sample of ^{23}Na - ^{40}K molecules exhibiting a large molecule-frame dipole moment (of 2.7 Debye) is produced. The quantum phase transition can be regarded as a novel phenomenon totally complementary to the well-known BCS-BEC crossover typical of Fermi systems [28] and the atomic-to-molecular BEC crossover in Bose systems [29]. The exploration of strong-correlation physics in degenerate Bose-Fermi mixtures, even if at the beginning, has been made possible in this way as well as,

with the extension of the innovative decompression technique, the achievement of a heteronuclear molecular BEC from Bose-Bose mixtures that suffer even more dramatically from losses when the condensation of both bosonic species takes place. Figure 1.4, being the phase diagram of the system under consideration, adequately sums up its main features.

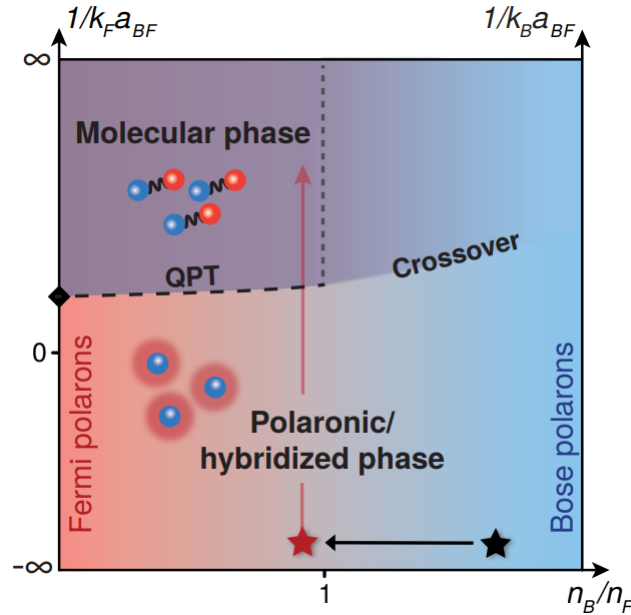


FIGURE 1.4: Phase diagram of degenerate Bose-Fermi mixtures as a function of the density ratio between bosons and fermions and the interaction strength. If the density ratio tends to zero we have the Fermi-polaron limit that exhibits a polaron-to-molecule transition (represented pictorially by the black diamond); if instead the same quantity tends to infinity, we reach the Bose-polaron limit with a smooth crossover [Figure reproduced from 27].

Let us conclude this section with a short digression on some technical aspects that have been outlined so far in the realization of the aforementioned experiments and that are strictly related to the framework of spectral weight functions $A(\mathbf{k}, \omega)$, which are, as stated in the introduction, the main focus of the thesis. It

has been pointed out that angle resolved photoemission spectroscopy (ARPES) is very useful when it comes to the determination of the fermionic spectral weight functions in electronic systems. Quite recent experiments on ^{40}K from the JILA group [30] have shown that it is possible to measure spectral weight functions by means of momentum resolved radio-frequency spectroscopy over a range of magnetic fields throughout the BCS-BEC crossover. The choice of ^{40}K as atomic species is on solid ground since, for the typical Fano-Feshbach resonance around 202 G, there are no competing resonances that could introduce complications from final state interactions. In this case, one is interested in signatures of pairing in a mixture of fermionic ^{40}K in two different hyperfine levels. A work conducted at the University of Chicago [31] has demonstrated that the momentum resolved radio-frequency spectroscopy has the same capabilities as that of ARPES and therefore can be used to measure the spectral function of ultracold Fermi gases. In particular, the momentum resolved radio-frequency spectrum turns out to be proportional to:

$$RF(\mathbf{k}, E) = \mathbf{k}^2 \int d^3\mathbf{r} A(\mathbf{k}, E - \mu(\mathbf{r}); \mathbf{r}) f(E - \mu(\mathbf{r})) \quad (1.2)$$

where $E = k^2/(2m) - \omega_\delta$ is the *single-particle* energy, $f(E - \mu(\mathbf{r}))$ is the Fermi function and ω_δ is the detuning of the radio-frequency probe with respect to the frequency of a specific atomic transition. Notice that in the (1.2) the average over the momentum has been deleted, hence the name of the technique (the trap average - on spatial coordinates - instead can be eliminated with another technique, called tomographic one, and introduced at MIT [32]). Furthermore, momentum resolved radio-frequency spectroscopy can be used to investigate the causes at the origin of double peak structure occurring in momentum-integrated radio-frequency spectra, in particular whether this behaviour is attributable to bound state effects or pairing. In the last two works cited, theoretical analysis and experimental results showed that the double peak structure seems to depend on unpaired atoms near the trap edge and on paired atoms near the trap center.

1.4 Latest experiments

The physics of ultracold gases is having a big boost nowadays because the implementation and the improvement of experimental techniques has led to confirmations or corrections of past theoretical predictions which, in turn, are now powered and encouraged by these new frontiers. For instance, a group of researchers [33] has obtained an increase up to 90% of the closed-channel fraction of Feshbach molecules of $^{23}\text{Na}^{40}\text{K}$ by using a magnetoassociation on the Fano-Feshbach resonance at a certain value of the magnetic field. This achievement has made possible better pump transition strengths to the absolute ground state as well as improved transfer efficiencies compared to more conventional techniques. Furthermore, filter cavities proved to be a useful method when it comes to the reduction of the detrimental laser noise.

Another work [34], both theoretical and experimental, has focused on the suppression of three-body loss at unitarity via Fermi degeneracy in a degenerate Bose-Fermi mixture. As said above, this technical issue is the cause of the failed realization of several experiments on Bose-Fermi mixtures. This problem has been analyzed in detail with a model based on RKKY interactions [35, 36, 37] that explains the suppression in the degenerate regime without using any fitting parameters and that lays the foundation for a deeper experimental investigation of Bose-Fermi mixtures at unitarity, whose theoretical study is addressed throughout this thesis.

The object of study of a very recent work [38] have been long-lived fermionic Feshbach molecules. The interest behind these molecules lies in the fact that they are suitable for the exploration of quantum matter with intense p -wave interactions. The main experimental problem is their very short lifetimes which make their measurements extremely difficult. The researchers studied the p -wave collisions of ultracold fermionic $^{23}\text{Na}^{40}\text{K}$ Feshbach molecules taking into account several scattering lengths and temperatures and noticed that an increase in the binding energy of the molecules leads to a much greater lifetime, about 20 times longer than that of ground-state molecules (specifically, the two-body loss coefficient reduces by three orders of magnitude). A regime in which the elastic collisions prevail on the inelastic ones has been identified by exploiting the scaling of these

collisions with the temperature and the scattering length, allowing the thermalization of the molecular sample. Moreover, this study, which is fundamental for producing a degenerate Fermi gas of Feshbach molecules (the dimer loss is significantly reduced after their formation by quenching the magnetic field into the regime of large binding energies), can be thought as a benchmark for solving the four-body problem which predicts the collisional behaviour in other heteronuclear molecules.

Last but not least, the unleashing of the potential of ultracold molecules requires cooling interacting molecular gases deeply into the quantum degenerate regime. Typically, collisions are unstable at the short range owing to the complexity of molecules and this results in a lack of cooling to quantum degeneracy (in three dimensions). One of the latest experiments [39] addressed this problem: using microwave shielding, the evaporative cooling of a 3D gas of fermionic $^{23}\text{Na}^{40}\text{K}$ molecules to well below the Fermi temperature has been achieved. This has been obtained by means of a repulsive barrier arranged by coupling rotational states with a blue-detuned circularly polarized microwave: by doing so, molecules were prevented from reaching short range. The large elastic-to-inelastic collision ratio, obtained by means of strong tunable dipolar interactions, made the cooling of the molecular gas possible, paving the way to future investigations of long-lived degenerate polar molecules and the consequent exploration of new quantum many-body phases with long-range anisotropic interactions.

Chapter 2

A theoretical approach to Bose-Fermi mixtures

In this Chapter we analyze Bose-Fermi mixtures in three dimensions at zero temperature exploiting the theoretical insight provided by Feynman's diagrams within the so-called *T-matrix* approach.

2.1 The model Hamiltonian

Now we are able to consider the system that will be our object of study, i.e. Bose-Fermi mixtures in three dimensions. We denote with n_F the density of single-component fermions, while n_B stands for the density of the bosons. The physical quantities that must be taken into account in this context are the effective range of the potential r_0 , the boson-fermion scattering length a_{BF} (where the subscript B is for bosons and the subscript F is for fermions) and the average interparticle distance l . The presence of a *broad* Fano-Feshbach resonance implies, as already pointed out in section 1.3, that $r_0 \ll l$ and $r_0 \ll a_{BF}$. In this framework, the boson-fermion interaction can be described by means of an attractive point-contact potential v_0^{BF} [40]. As a result, the minimal grand-canonical Hamiltonian turns out to be:

$$\begin{aligned}
H = & \sum_s \int d\mathbf{r} \psi_s^\dagger(\mathbf{r}) \left(-\frac{\nabla^2}{2m_s} - \mu_s \right) \psi_s(\mathbf{r}) \\
& + v_0^{BF} \int d\mathbf{r} \psi_B^\dagger(\mathbf{r}) \psi_F^\dagger(\mathbf{r}) \psi_F(\mathbf{r}) \psi_B(\mathbf{r}) \\
& + \frac{1}{2} \int d\mathbf{r} \int d\mathbf{r}' \psi_B^\dagger(\mathbf{r}) \psi_B^\dagger(\mathbf{r}') U_{BB}(\mathbf{r} - \mathbf{r}') \psi_B(\mathbf{r}') \psi_B(\mathbf{r})
\end{aligned} \tag{2.1}$$

where with $s =_{B,F}$ we denote the boson and fermion species respectively and with U_{BB} the boson-boson interaction. Notice that the reduced Planck constant and the Boltzmann one are set equal to 1 ($\hbar = k_B = 1$) and it will be so throughout the thesis. In (2.1) $\psi_s^\dagger(\mathbf{r})$ creates a particle of mass m_s and chemical potential μ_s , while $\psi_s(\mathbf{r})$ destroys a particle of mass m_s and chemical potential μ_s . It can be seen that the Hamiltonian has three contributions: the first is the free Hamiltonian which takes into account non-interacting bosons and fermions; the second is the boson-fermion interaction Hamiltonian, while the third is the boson-boson one. Fermion-fermion interaction is not considered owing to Pauli exclusion principle. The microscopic coupling v_0^{BF} can be expressed in terms of the boson-fermion scattering length a_{BF} as follows:

$$\frac{1}{v_0^{BF}} = \frac{m_r}{2\pi a_{BF}} - \int \frac{d\mathbf{k}}{(2\pi)^3} \frac{2m_r}{\mathbf{k}^2} \tag{2.2}$$

where \mathbf{k} is the momentum and $m_r = \frac{m_B m_F}{m_B + m_F}$ is the reduced mass of the boson-fermion system. Having written v_0^{BF} in this way, the ultraviolet divergences related to the contact interaction v_0^{BF} are suppressed. It is important to remark that, while the boson-fermion interaction is attractive and tunable by means of the Fano-Feshbach resonance, as previously stated, the boson-boson interaction is supposed to be weakly repulsive. As a consequence, there is no need to eliminate the corresponding ultraviolet divergence since it is treated at mean-field level (in this case we have $U_{BB}(\mathbf{r} - \mathbf{r}') = \frac{4\pi a_{BB}}{m_B} \delta(\mathbf{r} - \mathbf{r}')$, where a_{BB} is the boson-boson scattering length).

The inverse of the effective Fermi wave vector $k_F \equiv (3\pi^2 n)^{1/3}$ (where n is the

average density of fermions and bosons, i.e. $n = \frac{n_F + n_B}{2}$) provides a natural length scale of the system under consideration. An alternative possible description of k_F relates it directly to the density of the fermionic component: $k_F \equiv (6\pi^2 n_F)^{1/3}$. When $n_F = n_B$ the two definitions coincide. The strength of the interaction can be described by the dimensionless coupling parameter $g = (k_F a_{BF})^{-1}$. There are two main regimes: the weak-coupling limit corresponds to $g \ll -1$, whereas the molecular one, whose description is in terms of molecules and unpaired excess atoms (or particles) of the majority species interacting through a residual interaction which vanishes in the extreme molecular limit, is achieved whenever $g \gg 1$. In this second case, the radius of the bound state - that coincides with the scattering length a_{BF} , for $a_{BF} > 0$ - is significantly smaller than the average interparticle distance l . Typically we say that we are in the weak-coupling regime when $g \lesssim -2$ and in the strong-coupling one when $g \gtrsim 1$ (in particular, we refer to the $g \sim 0$ situation as unitarity). In both regimes, perturbation theory provides satisfactory results when it comes to the equations that rule the system, whilst in the intermediate situation, $-2 \lesssim g \lesssim 1$, the perturbative approach is no longer valid; as a result, a fully numerical solution of the problem is required.

2.2 *T*-matrix approach

The formalism is developed within the *T*-matrix approach: it consists of an approximate calculation which selects exclusively the class of Feynman's diagrams that collects all possible repeated boson-fermion interaction. Doing so, a ladder is formed and this is the reason why we refer to these diagrams as ladder diagrams. From a physical point of view, the *T*-matrix describes the interaction between particles before and after the scattering process, therefore it can be seen as a sort of scattering amplitude generalized in the medium which considers the background of the other particles when the scattering between two particles takes place. Actually, the choice of ladder diagrams is on solid ground since, for instance, these are prevalent in Bose-Fermi mixtures in the weak-coupling regime [41]; and also in the strong-coupling limit where the *T*-matrix class of diagrams

adequately describes the formation of molecules (composite fermions) reproducing the correct physical result [42]. Lastly, for a similar system to the one considered so far, that consists of a mixture of two components fermions in the presence of a Fano-Feshbach resonance, ladder diagrams give a good description through the entire resonance [43, 44].

In general, the choice of the self-energy diagrams should respond to the criterion that a single set of diagrams must reproduce the correct physical description of the weak-coupling limit as well as the strong-coupling one: in this way a proper theoretical framework for the entire resonance is provided.

Let us start the discussion with the Feynman's diagram for the T -matrix in the normal phase $\Gamma(\mathbf{P}, \Omega)$, which differs in some contributions from the condensed one, as we will see along this section. Physically speaking, the T -matrix in the normal phase stands for the propagator of boson-fermion pairs - as the name itself explains - in the normal phase. From a pictorial point of view, we have:

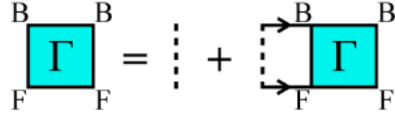


FIGURE 2.1: Feynman's diagram for the T -matrix in the normal phase.

which, after the use of Feynman's rules, produces:

$$\Gamma(\mathbf{P}, \Omega)^{-1} = \frac{1}{v_0^{BF}} + \int \frac{d\mathbf{p}}{(2\pi)^3} \frac{1 - \Theta(-\zeta_{\mathbf{P}-\mathbf{p}}^F) - \Theta(-\zeta_{\mathbf{p}}^B)}{\zeta_{\mathbf{P}-\mathbf{p}}^B + \zeta_{\mathbf{p}}^B - i\Omega} \quad (2.3)$$

In Figure 2.1 full lines stand for the bare boson (B) and fermion (F) Green's functions, while dashed lines represent the bare BF interactions. In (2.3) Ω is the frequency, \mathbf{P} and \mathbf{p} are the momenta and $\zeta_{\mathbf{k}}^s = \frac{\mathbf{k}^2}{2m_s} - \mu_s$ ([42], with an overall minus sign in the definition of Γ). At this stage, we can use Eq. (2.2) and obtain:

$$\Gamma(\mathbf{P}, \Omega)^{-1} = \frac{m_r}{2\pi a_{BF}} + \int \frac{d\mathbf{p}}{(2\pi)^3} \left(\frac{1 - \Theta(-\tilde{\zeta}_{\mathbf{P}-\mathbf{p}}^F) - \Theta(-\tilde{\zeta}_{\mathbf{p}}^B)}{\tilde{\zeta}_{\mathbf{P}-\mathbf{p}}^B + \tilde{\zeta}_{\mathbf{p}}^B - i\Omega} - \frac{2m_r}{\mathbf{p}^2} \right) \quad (2.4)$$

As stated before, we will always consider the zero temperature limit throughout the thesis; if it had not been so, we would have obtained:

$$\Gamma(\mathbf{P}, \Omega)^{-1} = \frac{m_r}{2\pi a_{BF}} + \int \frac{d\mathbf{p}}{(2\pi)^3} \left(\frac{1 - f(\tilde{\zeta}_{\mathbf{P}-\mathbf{p}}^F) - b(\tilde{\zeta}_{\mathbf{p}}^B)}{\tilde{\zeta}_{\mathbf{P}-\mathbf{p}}^B + \tilde{\zeta}_{\mathbf{p}}^B - i\Omega} - \frac{2m_r}{\mathbf{p}^2} \right) \quad (2.5)$$

Here, $f(x)$ and $b(x)$ are the Fermi and Bose distribution functions at temperature T , respectively ($f(x) = 1/(e^{x/T} + 1)$ and $b(x) = 1/(e^{x/T} - 1)$). Comparing directly Eqs. (2.4) and (2.5) we notice that the zero temperature limit of the Fermi and Bose distributions leads to the Θ functions, as it should be. Now we can define:

$$I_F(\mathbf{P}, \Omega) \equiv \int \frac{d\mathbf{p}}{(2\pi)^3} \frac{1 - \Theta(-\tilde{\zeta}_{\mathbf{P}-\mathbf{p}}^F) - \Theta(-\tilde{\zeta}_{\mathbf{p}}^B)}{\tilde{\zeta}_{\mathbf{P}-\mathbf{p}}^F - \tilde{\zeta}_{\mathbf{p}}^B - i\Omega} \quad (2.6)$$

and the strong-coupling limit Γ^{SC} of Γ :

$$\Gamma^{\text{SC}}(\mathbf{P}, \Omega)^{-1} = \frac{m_r}{2\pi a_{BF}} - \frac{m_r^{3/2}}{\sqrt{2\pi}} \sqrt{\frac{P^2}{2M} - 2\mu - i\Omega} \quad (2.7)$$

where $M = m_B + m_F$ and $\mu = \frac{\mu_B + \mu_F}{2}$. The contribution that comes from the integration of $\Theta(-\tilde{\zeta}_{\mathbf{p}}^B)$ is set to zero because the calculation scheme requires that the bosonic chemical potential μ_B is set to zero, when computing Γ and Γ^{SC} , whenever it is positive. This is to correct unphysical features arising when $\mu_B > 0$ is used in a bare bosonic Green's function. A more refined approach would require some sort of self-consistency in this case. We stress, however, that for the cases considered in the present work μ_B will be always negative. Now, let us consider the fermionic chemical potential μ_F : when $\mu_F \leq 0$, I_F is zero. More generally, also for μ_F , I_F can be evaluated in a closed form since the integration of I_F with the

Fermi function in (2.4) yields:

$$I_F(\mathbf{P}, \Omega) = \frac{m_B(k_{\mu F}^2 - k_{\mathbf{P}}^2 - k_{\Omega}^2)}{8\pi^2 P} \log \left[\frac{(k_{\mu F} + k_{\mathbf{P}})^2 - k_{\Omega}^2}{(k_{\mu F} - k_{\mathbf{P}})^2 - k_{\Omega}^2} \right] - \frac{m_r k_{\Omega}}{4\pi^2} \log \left[\frac{(k_{\mu F} + k_{\Omega})^2 - k_{\mathbf{P}}^2}{k_{\mathbf{P}}^2 - (k_{\mu F} - k_{\Omega})^2} \right] - i\pi s \operatorname{sgn}(\Omega) + \frac{m_r k_{\mu F}}{2\pi^2} \quad (2.8)$$

where $k_{\mu F} \equiv \sqrt{2m_F \mu_F}$, $k_{\mathbf{P}} \equiv \frac{m_F}{M} P$ and $k_{\Omega} \equiv \sqrt{(2m_r)(-\frac{\mathbf{P}^2}{2M} + 2\mu + i\Omega)}$.

Let us consider the condensed phase which is the case of interest to the present thesis: in this context, as stated before, we admit in the system the phenomenon of Bose-Einstein condensation. The corresponding Feynman's diagram for the T -matrix is the following:

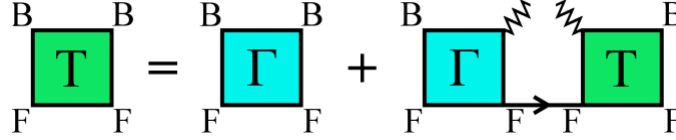


FIGURE 2.2: Feynman's diagram for the T -matrix for the condensed phase.

In Figure 2.2, in addition to the graphical considerations already made with regard to the normal phase, zig-zag lines represent condensate factors $\sqrt{n_0}$, where n_0 is the condensate density. Correspondingly, we have:

$$T(\mathbf{P}, \Omega) = \Gamma(\mathbf{P}, \Omega) + \Gamma(\mathbf{P}, \Omega) n_0 G_F^0(\mathbf{P}, \Omega) T(\mathbf{P}, \Omega) \quad (2.9)$$

where $G_F^0(\mathbf{P}, \Omega) = \frac{1}{i\Omega - \zeta_{\mathbf{P}}^F}$ is the bare fermion Green's function. Solving for $T(\mathbf{P}, \Omega)$, we get the following solution:

$$T(\mathbf{P}, \Omega) = \frac{1}{\Gamma(\mathbf{P}, \Omega)^{-1} - n_0 G_F^0(\mathbf{P}, \Omega)} \quad (2.10)$$

2.3 Fermionic and bosonic self-energies

After writing the expression for the T -matrix in the condensed phase, it is time to compute the bosonic and the fermionic self-energies since they are, as we will see in a while, a necessary step when dealing with spectral weight functions. From a physical point of view, the self-energy of a single particle represents (in many-body theory) the extra energy that the particle acquires through the interactions with all other particles in the system.

The fermionic self-energy Σ_F depends solely on the coupling with bosons. Here are the Feynman's diagrams:

$$\Sigma_F = \text{Diagram 1} + \text{Diagram 2}$$

FIGURE 2.3: Feynman's diagrams for Σ_F . As stated previously, zig-zag lines correspond to condensate factors $\sqrt{n_0}$.

which, after the application of Feynman's rules, read:

$$\Sigma_F(\mathbf{k}, \omega) = n_0 \Gamma(\mathbf{k}, \omega) - \int \frac{d\mathbf{P}}{(2\pi)^3} \int \frac{d\Omega}{2\pi} T(\mathbf{P}, \Omega) G_B^0(\mathbf{P} - \mathbf{k}, \Omega - \omega) \quad (2.11)$$

When dealing with fermionic self-energy, there is an aspect which is worth pointing out: the T -matrix can be closed in the diagrammatic form with a boson propagator or with two condensate insertions; this second option would lead to improper self-energy diagrams [45]. Proper diagrams instead, whose graphs cannot be cut in two by slicing a single propagator, are obtained by substituting T with Γ in this contribution (see Figure 2.3).

Now let us focus on the bosonic component: if we admit that there is no coupling with fermions and for a boson gas parameter $\eta = n_B a_{BB}^3 \ll 1$, a description

for $T = 0$ is given by Bogoliubov theory, which leads to the values of $4\pi a_{BB}n_0/m_B$ and $8\pi a_{BB}n_0/m_B$ for the anomalous and normal self-energies, respectively. Since it has been shown [46, 47] that pairing correlations between bosons and fermions can be included in an accurate way by a T -matrix type of self-energy, the extension of the latter to the condensed phase is straightforwardly realized: it is sufficient to add to the Bogoliubov term - concerning the normal self-energy - the T -matrix contribution $\Sigma_{BF}(\mathbf{k}, \omega)$ given by:

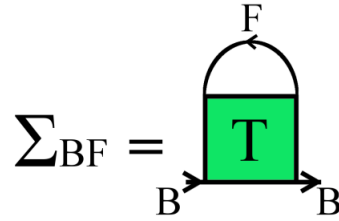


FIGURE 2.4: Feynman's diagrams for Σ_{BF} . As stated previously, full lines stand for bare bosonic and fermionic Green's functions.

which, according to Feynman's rules, turns out to be:

$$\Sigma_{BF}(\mathbf{k}, \omega) = \int \frac{d\mathbf{P}}{(2\pi)^3} \int \frac{d\Omega}{2\pi} T(\mathbf{P}, \Omega) G_F^0(\mathbf{P} - \mathbf{k}, \Omega - \omega) \quad (2.12)$$

Notice that the T -matrix is closed in a diagrammatic form with a fermion propagator - the loop carries a minus sign - so that it can be regarded as an effective interaction with regard to the single boson. After adding the two contributions together, we get the full bosonic normal self-energy $\Sigma_B(\mathbf{k}, \omega)$ which reads:

$$\Sigma_B(\mathbf{k}, \omega) = 2\Sigma_{12} + \int \frac{d\mathbf{P}}{(2\pi)^3} \int \frac{d\Omega}{2\pi} T(\mathbf{P}, \Omega) G_F^0(\mathbf{P} - \mathbf{k}, \Omega - \omega) \quad (2.13)$$

with $\Sigma_{12} = 4\pi a_{BB}n_0/m_B$. In the (2.13) the bosonic chemical potential μ_B is set to zero if it is positive. A very useful relation, known as Hugenholtz-Pines theorem [48], holds, connecting this quantity with the bosonic self-energy:

$$\mu_B = \Sigma_B(\mathbf{k} = \mathbf{0}, \omega = 0) - \Sigma_{12} \quad (2.14)$$

2.4 Green's functions, momentum distributions and density

Knowing the bare fermionic Green's function $G_F^0(\mathbf{k}, \omega) = 1/(i\omega - \zeta_{\mathbf{k}}^F)$ and the fermionic self-energy $\Sigma_F(\mathbf{k}, \omega)$, it is possible to determine the dressed fermionic Green's function $G_F(\mathbf{k}, \omega)$ via the Dyson's equation:

$$G_F(\mathbf{k}, \omega) = \frac{1}{G_F^{0-1}(\mathbf{k}, \omega) - \Sigma_F(\mathbf{k}, \omega)} \quad (2.15)$$

The dressed bosonic Green's function is more elaborate since the condensed phase related to the Bose-Einstein condensation must be taken into consideration. After some calculations [50] and the application of the Dyson's equation, we get:

$$G_B(\mathbf{k}, \omega) = \frac{i\Omega + \zeta_{\mathbf{k}}^B + \Sigma_B(-\mathbf{k}, -\omega)}{[i\Omega + \zeta_{\mathbf{k}}^B + \Sigma_B(-\mathbf{k}, -\omega)][i\omega - \zeta_{\mathbf{k}}^B - \Sigma_B(\mathbf{k}, \omega)] + \Sigma_{12}^2} \quad (2.16)$$

The integration of the dressed Green's functions over frequencies provides the momentum distribution functions, which are:

$$n_F(\mathbf{k}) = \int \frac{d\omega}{2\pi} G_F(\mathbf{k}, \omega) e^{i\omega 0^+} \quad (2.17)$$

and:

$$n_B(\mathbf{k}) = - \int \frac{d\omega}{2\pi} G_B(\mathbf{k}, \omega) e^{i\omega 0^+} \quad (2.18)$$

At this stage, it is possible to determine the fermion number density as well as the out-of-condensate boson one by performing the integration over momenta of the (2.17) and (2.18), respectively:

$$n_F = \int \frac{d\mathbf{k}}{(2\pi)^3} n_F(\mathbf{k}) \quad (2.19)$$

$$n'_B = \int \frac{d\mathbf{k}}{(2\pi)^3} n_B(\mathbf{k}) \quad (2.20)$$

The total boson density turns out to be:

$$n_B = n_0 + n'_B \quad (2.21)$$

i.e. the sum of the density of the condensed bosons and the density of the bosons out of the condensate. In the following we will study systems characterized by majority of fermions or with $n_F = n_B$, therefore it is customary to introduce the ratio between boson and fermion densities, also known as bosonic concentration x :

$$x \equiv \frac{n_B}{n_F} \quad (2.22)$$

Even if we will not focus on the opposite case, represented by a system in which bosons are the majority species, previous considerations can be straightforwardly extended by taking into account the fermionic concentration, defined as:

$$y \equiv \frac{n_F}{n_B} \quad (2.23)$$

There are three different scenarios which are worth mentioning: the first is the *density-balanced* system in which $x = y = 1$, while the two remaining are known as *polaron* limit: if a single bosonic impurity is immersed in a Fermi sea, then $x \rightarrow 0$ (Fermi-polaron limit); if instead in the Bose-Fermi mixture the single fermionic impurity is immersed in a Bose-Einstein condensate, $y \rightarrow 0$ and we refer to this situation as the Bose-polaron limit.

2.5 Analytic continuation and poles of the retarded T -matrix

The calculation of the spectral weight functions requires the analytic continuation from the imaginary frequency axis to the real one. This is achieved via the replacement:

$$i\omega \rightarrow \tilde{\omega} + i0^+ \quad (2.24)$$

where the symbol 0^+ denotes an infinitesimally small and positive constant and the \sim -symbol indicates that the frequency is real. Physical quantities characterized by the above substitution are called *retarded* and are denoted in this way:

$$X^R, \quad (2.25)$$

where X stands for a generic quantity (e.g. T -matrix, Green's function, etc.) while the superscript R represents the analytic continuation.

The fermionic and the bosonic spectral functions can be expressed in terms of the imaginary part of the retarded Green's functions as follows:

$$A_s(\mathbf{k}, \tilde{\omega}) = -\frac{1}{\pi} \text{Im} G_s^R(\mathbf{k}, \tilde{\omega}) \quad (2.26)$$

and they satisfy the sum rule:

$$\int_{-\infty}^{\infty} d\tilde{\omega} A_s(\mathbf{k}, \tilde{\omega}) = 1 \quad (2.27)$$

In particular, $A_F(\mathbf{k}, \tilde{\omega})$ is always positive but this is not true for the bosonic spectral weight function: in fact, we have $\text{sgn}(\tilde{\omega}) A_B(\mathbf{k}, \tilde{\omega}) \geq 0$. The proof starts from the Lehmann representation (see [45], Chapter 9) of the two spectral weight functions which, in the $T = 0$ case, turns out to be:

$$A_{B,F}(\mathbf{k}, \tilde{\omega}) = \begin{cases} \sum_n |\langle n | (c_{\mathbf{k}}^s)^\dagger | \Psi_0 \rangle|^2 \delta(\tilde{\omega} - \epsilon_n^{N_s+1, N_s}) & \tilde{\omega} > 0 \\ \sum_n \mp |\langle n | c_{\mathbf{k}}^s | \Psi_0 \rangle|^2 \delta(\tilde{\omega} + \epsilon_n^{N_s-1, N_s}) & \tilde{\omega} < 0 \end{cases} \quad (2.28)$$

In Eq. (2.28) the positive sign of the second expression stands for the fermionic component, while the negative for the bosonic one. The sum is extended over all the eigenstates $|n\rangle$ of the Hamiltonian that have a nonvanishing overlap with the state that is obtained by subtracting - for $\tilde{\omega} < 0$ - or adding - for $\tilde{\omega} > 0$ - a particle of species s (with momentum \mathbf{k}) from - or to - the ground state Ψ_0 of the system characterized by the presence of N_s particles of the species s and $N_{\bar{s}}$ particles of the other species. Consequently, these states belong to the Hilbert space with $N_s \pm 1$ and $N_{\bar{s}}$ particles of the two different species and their excitation energies are $\epsilon_n^{N_s \pm 1, N_{\bar{s}}}$. The negative sign of the bosonic spectral weight function for negative frequency ensures the positivity of the bosonic momentum distribution function. Therefore, considering as always the $T = 0$ case, we have:

$$n_{B,F}(\mathbf{k}) = \mp \int_{-\infty}^0 d\tilde{\omega} A_{B,F}(\mathbf{k}, \tilde{\omega}) \quad (2.29)$$

Equations (2.29) are clearly obtained by the finite temperature momentum distribution functions $n_F(\mathbf{k}) = \int_{-\infty}^{\infty} f(\tilde{\omega}) A_F(\mathbf{k}, \tilde{\omega})$ and $n_B(\mathbf{k}) = \int_{-\infty}^{\infty} b(\tilde{\omega}) A_B(\mathbf{k}, \tilde{\omega})$, where $f(\tilde{\omega})$ and $b(\tilde{\omega})$ are the Fermi-Dirac and the Bose-Einstein distribution, respectively $\left(f(\tilde{\omega}) = \frac{1}{e^{\beta\tilde{\omega}} + 1}$ and $b(\tilde{\omega}) = \frac{1}{e^{\beta\tilde{\omega}} - 1}$, with $\beta = \frac{1}{T}$).

A direct inspection of Eq. (2.26) suggests that the determination of the retarded Green's functions is crucial. Operationally, one must consider the equations - already written previously - that lead to the dressed Green's functions and simply perform the analytic continuation to the physical quantities involved, as shown in the present section. In order to compute the retarded Green's functions, it is useful to introduce the spectral representation for the many-body T -matrix in the condensed phase which reads:

$$T(\mathbf{P}, \Omega) = - \int \frac{d\omega'}{\pi} \frac{\text{Im}T^R(\mathbf{P}, \omega')}{i\Omega - \omega'} \quad (2.30)$$

Here, $T^R(\mathbf{P}, \omega')$ is obtained from Eq. (2.10) for $T(\mathbf{P}, \Omega)$ with the replacement $i\Omega \rightarrow \omega' + i0^+$ (ω' real). Now we are ready to plug Eq. (2.30) in the fermionic and bosonic self-energies. Let us start with the fermionic case. Recall Eq. (2.11):

$$\Sigma_F(\mathbf{k}, \omega) = n_0 \Gamma(\mathbf{k}, \omega) - \int \frac{d\mathbf{P}}{(2\pi)^3} \int \frac{d\Omega}{2\pi} T(\mathbf{P}, \Omega) G_B^0(\mathbf{P} - \mathbf{k}, \Omega - \omega) \quad (2.31)$$

The insertion of Eq. (2.30) in Eq. (2.31), as well as writing the bare bosonic Green's function explicitly, leads to:

$$\Sigma_F(\mathbf{k}, \omega) = n_0 \Gamma(\mathbf{k}, \omega) + \int \frac{d\mathbf{P}}{(2\pi)^3} \int \frac{d\Omega}{2\pi} \int \frac{d\omega'}{\pi} \frac{\text{Im}T^R(\mathbf{P}, \omega')}{i\Omega - \omega'} \frac{1}{i\Omega - i\omega - \xi_{\mathbf{P}-\mathbf{k}}^B} \quad (2.32)$$

The integration over Ω can be performed by a contour integration, yielding:

$$\Sigma_F(\mathbf{k}, \omega) = n_0 \Gamma(\mathbf{k}, \omega) - \int \frac{d\mathbf{P}}{(2\pi)^3} \int_{-\infty}^0 \frac{d\omega'}{\pi} \frac{\text{Im}T^R(\mathbf{P}, \omega')}{i\omega - \omega' + \xi_{\mathbf{P}-\mathbf{k}}^B + i0^+} \quad (2.33)$$

where we used $\xi_{\mathbf{P}-\mathbf{k}}^B$ since $\mu_B \leq 0$. The analytic continuation $i\omega \rightarrow \tilde{\omega} + i0^+$ then yields in Eq. (2.32):

$$\Sigma_F^R(\mathbf{k}, \tilde{\omega}) = n_0 \Gamma^R(\mathbf{k}, \tilde{\omega}) - \int \frac{d\mathbf{P}}{(2\pi)^3} \int_{-\infty}^0 \frac{d\omega'}{\pi} \frac{\text{Im}T^R(\mathbf{P}, \omega')}{\tilde{\omega} - \omega' + \xi_{\mathbf{P}-\mathbf{k}}^B + i0^+} \quad (2.34)$$

Similar reasoning can be extended to the bosonic case. Recalling Eq. (2.13):

$$\Sigma_B(\mathbf{k}, \omega) = 2\Sigma_{12} + \int \frac{d\mathbf{P}}{(2\pi)^3} \int \frac{d\Omega}{2\pi} T(\mathbf{P}, \Omega) G_F^0(\mathbf{P} - \mathbf{k}, \Omega - \omega) \quad (2.35)$$

Then, the spectral representation of the many-body T -matrix and the bare fermionic Green's function in explicit form provide:

$$\Sigma_B(\mathbf{k}, \omega) = 2\Sigma_{12} - \int \frac{d\mathbf{P}}{(2\pi)^3} \int \frac{d\Omega}{2\pi} \int_{-\infty}^{\infty} \frac{d\omega'}{\pi} \frac{\text{Im}T^R(\mathbf{P}, \omega')}{i\Omega - \omega'} \frac{1}{i\Omega - i\omega - \xi_{\mathbf{P}-\mathbf{k}}^F} \quad (2.36)$$

The integration over Ω , followed by the analytic continuation $i\omega \rightarrow \tilde{\omega} + i0^+$ yields in this case:

$$\begin{aligned} \Sigma_B^R(\mathbf{k}, \tilde{\omega}) = 2\Sigma_{12} + \int \frac{d\mathbf{P}}{(2\pi)^3} \left[\int_{-\infty}^{\infty} \frac{d\omega'}{\pi} \frac{\Theta(-\tilde{\zeta}_{\mathbf{P}-\mathbf{k}}^F) \text{Im}T^R(\mathbf{P}, \omega')}{\omega - \omega' + \tilde{\zeta}_{\mathbf{P}-\mathbf{k}}^F + i0^+} \right. \\ \left. - \int_{-\infty}^0 \frac{d\omega'}{\pi} \frac{\text{Im}T^R(\mathbf{P}, \omega')}{\omega - \omega' + \tilde{\zeta}_{\mathbf{P}-\mathbf{k}}^F + i0^+} \right] \end{aligned} \quad (2.37)$$

The integrals obtained so far are computationally demanding when it comes to the numerical calculation program, therefore they can be recast in a more manageable way. In order to do so, it is important determining the poles of the retarded T -matrix. In general, these latter are defined by the following equation:

$$\text{Re}T^R(\mathbf{P}, \Omega(P))^{-1} = 0 \quad (2.38)$$

when, at the same time:

$$\text{Im}T^R(\mathbf{P}, \Omega(P))^{-1} = 0 \quad (2.39)$$

In practice, we have to consider the real part of the inverse retarded T -matrix and then apply a suitable method in order to find the zeroes of the function: in the present case the bisection method was used (see Appendix B for further details). Once $\Omega(\mathbf{P})$ is determined as a solution of Eq. (2.38), one has to check that also Eq. (2.39) is satisfied (i.e. $\Omega(\mathbf{P})$ does not belong to the region where $\text{Im}T^R(\mathbf{P}, \Omega(P))^{-1} \neq 0$). Depending on the values of the coupling strength, Eq. (2.38) may lead to one or two dispersions, which we call $\Omega_{T1}(\mathbf{P})$ and $\Omega_{T2}(\mathbf{P})$. The first one, which is always present, describes the propagation and repeated scattering of a fermion and a boson which are unpaired. The second one, $\Omega_{T2}(\mathbf{P})$, which appears above a certain coupling strength, describes the propagation of a boson and a fermion which are bound together in a "molecular" state. In light of these considerations, the lowest value of the coupling for which we assist at the appearance of the second pole is nothing but the coupling that is responsible for the conversion of correlated boson-fermion pairs into molecular bound states. It will be important to determine the dispersions of these poles, namely $\Omega_{T1}(P)$ and

$\Omega_{T2}(P)$. The dispersions cross zero at Fermi momenta, i.e. $\Omega_{T1}(P_{T1}^0) = 0$ and $\Omega_{T2}(P_{T2}^0) = 0$. The two poles are responsible for the jumps in the integrand functions of P of the fermionic and bosonic retarded self-energies and that is the reason why they are suitable to optimize calculations. In a similar way, one obtains the dispersion $\Omega_{\Gamma}(P)$ corresponding to the pole of Γ^R , with the momentum P_{Γ}^0 given by the solution of $\Omega_{\Gamma}(P) = 0$. Its value is crucial since it is typically involved in the numerical calculation of the steps of the fermionic momentum distribution function $n_F(k)$ (above a certain value of the coupling parameter g).

2.6 Poles of the retarded Green's function and quasi-particle residue

As for the retarded T -matrix, it is useful to look for the poles of the fermionic Green's function $G_F^R(\mathbf{k}, \omega)$. The equation for this type of poles reads:

$$\text{Re}G_F^R(\mathbf{k}, \omega(k))^{-1} = 0 \quad (2.40)$$

when:

$$\text{Im}G_F^R(\mathbf{k}, \omega(k))^{-1} = 0 \quad (2.41)$$

The dispersions of the poles will cross zero for possibly two values of momentum k that are called k_{F1} and k_{F2} , similarly to P_{T1}^0 and P_{T2}^0 . The fermionic momentum distribution function $n_F(\mathbf{k})$ will have a jump for this values of momentum (k_{F1} and k_{F2}). As in the case of the poles of the retarded T -matrix in the condensed phase, k_{F1} exists for every coupling and concentration, while k_{F2} is found only in systems in which fermions are the majority species and only above a certain value of the coupling parameter g [49].

When $k = P_{\Gamma}^0$ the function $\text{Re}G_F^R(k, \omega(k))^{-1}$ exhibits a divergence since at such value of momentum the term $n_0\Gamma^R(k, \omega(k))$ has a pole. The necessary condition that leads to the existence of the Fermi step k_{F2} is that, in turn, P_{Γ}^0 exists. In summary, when there is only one solution, this is called k_{F1} ; otherwise, when two solutions are found, we have the following ordering: $k_{F2} < P_{\Gamma}^0 < k_{F1}$.

The quasi-particle residue $Z_p(\mathbf{k})$, with $p = 1, 2$ according to which step of Fermi

momentum (k_{F1} or k_{F2}) is taken into consideration, determines the size of the jump. In fact, we associate to k_{F1} and k_{F2} the magnitude of the jumps Z_1 and Z_2 , which are defined as:

$$Z_p(\mathbf{k}) = \left| 1 - \frac{\partial}{\partial \omega} \text{Re} \Sigma_F^R(\mathbf{k}, \tilde{\omega}) \right|_{\tilde{\omega}=\omega_1(\mathbf{k})}^{-1} \quad (2.42)$$

with $\omega_1(\mathbf{k}) = \zeta_{\mathbf{k}} + \text{Re} \Sigma_F^R(\mathbf{k}, \omega_1(\mathbf{k}))$. In the Appendix A some theoretical aspects of the quasi-particle residue (or weight) are developed more in detail since they are functional to our discussion.

2.7 Manipulation of the integrals involved in the fermionic and bosonic retarded self-energies

In this section, as anticipated, we perform some calculations in order to simplify the computation of the integrals related to the fermionic and bosonic retarded self-energies, whose expressions have already been derived (see (2.34) and (2.37), respectively). From now on, we will drop the \sim symbol to explicitly indicate real frequencies since we will work only with retarded Green's functions (or spectral weight functions) for which the frequency is always real. In addition, in the following expressions we use dimensionless variables, so, energy and frequencies are in units of $E_F = k_F^2/2m_F$, momenta in units of k_F and masses in units of m_F . Let us first deal with the fermionic case since it is simpler. After changing to spherical coordinates, and integrating over the angles, we have:

$$\begin{aligned} \Sigma_F^R(\mathbf{k}, \omega) &= n_0 \Gamma^R(\mathbf{k}, \omega) - \frac{m_B}{8\pi^3 k} \int_0^\infty dPP \int_{-\infty}^0 d\omega' \text{Im} T^R(\mathbf{P}, \omega') \\ &\times \log \left[\frac{\omega - \omega' + \frac{(\mathbf{P}-\mathbf{k})^2}{m_B} - \mu_B + i0^+}{\omega - \omega' + \frac{(\mathbf{P}+\mathbf{k})^2}{m_B} - \mu_B + i0^+} \right] \end{aligned} \quad (2.43)$$

Now it is useful to introduce the variable:

$$\rho_F = \frac{\omega - \omega' + \frac{(\mathbf{P}-\mathbf{k})^2}{m_B} - \mu_B}{\omega - \omega' + \frac{(\mathbf{P}+\mathbf{k})^2}{m_B} - \mu_B} \quad (2.44)$$

so that, after taking properly into account the $i0^+$ term, Eq. (2.43) becomes:

$$\begin{aligned} \Sigma_F^R(\mathbf{k}, \omega) &= n_0 \Gamma^R(\mathbf{k}, \omega) - \frac{m_B}{8\pi^3 k} \int_0^\infty dPP \int_{-\infty}^0 d\omega' \text{Im} T^R(\mathbf{P}, \omega') \\ &\quad \times (\ln|\rho_F| + i\pi\Theta(-\rho_F)) \end{aligned} \quad (2.45)$$

The integral over the frequency variable can be performed analytically taking into account the delta-like contributions which are determined by the poles $\omega_T(P)$ of the retarded T -matrix. Indeed, by inspection of Eq. after the replacement $i\Omega \rightarrow \omega' + i0^+$, it is easy to verify that the threshold frequency $\omega_0(P)$ above which $\text{Im} I_F^R(P, \omega') \neq 0$ is always positive. This is also the threshold frequency for $\text{Im} T^R(\mathbf{P}, \omega')$. As a consequence, the only contributions to the frequency integral in Eq. (2.45) come from the poles (δ -like contributions) of $T^R(P, \omega')$ with dispersions $\omega_T(P)$. In this way, one obtains:

$$\begin{aligned} \Sigma_F^R(\mathbf{k}, \omega) &= n_0 \Gamma^R(\mathbf{k}, \omega) - \frac{m_B}{8\pi^2 k} \int_0^{k_T} dPP [(\ln|\rho_F| + i\pi\Theta(-\rho_F))]_{\omega'=\omega_T(P)} \\ &\quad \times \left| \frac{\partial \text{Re}[T^R(\mathbf{P}, \omega')^{-1}]}{\partial \omega'} \right|_{\omega'=\omega_T(P)}^{-1} \end{aligned} \quad (2.46)$$

Notice that the integral over the momentum P is limited by the momentum P_{T1}^0 or P_{T2}^0 , which is the last value accessible when taking into consideration $\omega' \leq 0$, and represents the point at which the dispersion curve of the composite fermion reaches the zero. This corresponds to the jump in the momentum distribution function of the composite fermions, namely the Fermi momentum of the Fermi

sphere of the composite fermions.

Let us now deal with the bosonic case which is more involved. Recall Eq. (2.37). After defining:

$$\begin{aligned}\Sigma_B^R(\mathbf{k}, \omega)^I &\equiv \int \frac{d\mathbf{P}}{(2\pi)^3} \int_{-\infty}^{\infty} \frac{d\omega'}{\pi} \frac{\Theta(-\zeta_{\mathbf{P}-\mathbf{k}}^F) \text{Im}T^R(\mathbf{P}, \omega')}{\omega - \omega' + \zeta_{\mathbf{P}-\mathbf{k}}^F + i0^+} \\ &= \int \frac{d\mathbf{P}}{(2\pi)^3} \Theta(\mu_F - (\mathbf{P} - \mathbf{k})^2) \int_{-\infty}^{\infty} \frac{d\omega'}{\pi} \frac{\text{Im}T^R(\mathbf{P}, \omega')}{\omega - \omega' + \zeta_{\mathbf{P}-\mathbf{k}}^F + i0^+}\end{aligned}\quad (2.47)$$

and:

$$\Sigma_B^R(\mathbf{k}, \omega)^{II} \equiv - \int \frac{d\mathbf{P}}{(2\pi)^3} \int_{-\infty}^0 \frac{d\omega'}{\pi} \frac{\text{Im}T^R(\mathbf{P}, \omega')}{\omega - \omega' + \zeta_{\mathbf{P}-\mathbf{k}}^F + i0^+}\quad (2.48)$$

we can write:

$$\Sigma_B^R(\mathbf{k}, \omega) = 2\Sigma_{12} + \Sigma_B^R(\mathbf{k}, \omega)^I + \Sigma_B^R(\mathbf{k}, \omega)^{II}\quad (2.49)$$

Equation (2.48) is very similar to its fermionic counterpart: therefore it is sufficient to follow an analogous procedure. Thus, let us move to spherical coordinates as done previously. We get:

$$\begin{aligned}\Sigma_B^R(\mathbf{k}, \omega)^{II} &= \frac{1}{8\pi^3 k} \int_0^\infty dPP \int_{-\infty}^0 d\omega' \text{Im}T^R(\mathbf{P}, \omega') \\ &\quad \times \log \left[\frac{\omega - \omega' + (\mathbf{P} - \mathbf{k})^2 - \mu_F + i0^+}{\omega - \omega' + (\mathbf{P} + \mathbf{k})^2 - \mu_F + i0^+} \right]\end{aligned}\quad (2.50)$$

Then, we define:

$$\rho_B^{II} = \frac{\omega - \omega' + (\mathbf{P} - \mathbf{k})^2 - \mu_F}{\omega - \omega' + (\mathbf{P} + \mathbf{k})^2 - \mu_F}\quad (2.51)$$

in order to reach the following expression for $\Sigma_B^R(\mathbf{k}, \omega)^{II}$:

$$\Sigma_B^R(\mathbf{k}, \omega)^{II} = \frac{1}{8\pi^3 k} \int_0^\infty dPP \int_{-\infty}^0 d\omega' \text{Im}T^R(\mathbf{P}, \omega')$$

$$\times (\ln|\rho_B^{II}| + i\pi\Theta(-\rho_B^{II})) \quad (2.52)$$

The analytical calculation of the integral on the frequency variable leads to:

$$\begin{aligned} \Sigma_B^R(\mathbf{k}, \omega)^{II} &= \frac{1}{8\pi^2 k} \int_0^{k_T} dPP[(\ln|\rho_B^{II}| + i\pi\Theta(-\rho_B^{II}))]_{\omega'=\omega_T(P)} \\ &\times \left| \frac{\partial \text{Re}[T^R(\mathbf{P}, \omega')^{-1}]}{\partial \omega'} \right|_{\omega'=\omega_T(P)}^{-1} \end{aligned} \quad (2.53)$$

Note that in the above equation we have used again ${}_0(P) > 0$. A suitable compact form cannot be achieved for $\Sigma_B^R(\mathbf{k}, \omega)^I$ so we must proceed in another way. It is crucial to point out that the step function $\Theta(\mu_F - (\mathbf{P} - \mathbf{k})^2)$ is responsible for the restriction of the domain of integration over the momentum \mathbf{P} ; furthermore, it provides two different expressions - based on the sign of $k_{\mu_F} - k$, where $k_{\mu_F} \equiv \sqrt{\mu_F}$ - that we are going to analyze. The computation of the frequency integral requires the determination of the ordering between the three different momenta P_T , $|k_{\mu_F} - k|$ and $k_{\mu_F} + k$ which we will encounter in the following. Along the lines of what has been done with regard to the quantities ρ_F and ρ_B^{II} , let us define:

$$\rho_B^I = \frac{\omega - \omega' + (\mathbf{P} - \mathbf{k})^2 - \mu_F}{\omega - \omega'} \quad (2.54)$$

We distinguish two cases:

- $k_{\mu F} < k$

The expression for $\Sigma_B^R(\mathbf{k}, \omega)^I$ turns out to be:

$$\begin{aligned} \Sigma_B^R(\mathbf{k}, \omega)^I &= \frac{1}{(2\pi)^3 k} \int_{|k_{\mu F}-k|}^{k_{\mu F}+k} dPP \left\{ \pi [\ln |\rho_B^I|^{-1} - i\pi \Theta(-\rho_B^I)]_{\omega'=\omega_T(P)} \right. \\ &\times \left. \left| \frac{\partial \text{Re}[T^R(\mathbf{P}, \omega')^{-1}]}{\partial \omega'} \right|_{\omega'=\omega_T(P)}^{-1} + \int_{\omega_0(P)}^{\infty} d\omega' \text{Im} T^R(\mathbf{P}, \omega) [\ln |\rho_B^I|^{-1} - i\pi \Theta(-\rho_B^I)] \right\} \end{aligned} \quad (2.55)$$

As before, $\omega_T(P)$ represents the solution of the equation $\text{Re}[T^R(\mathbf{P}, \omega')^{-1}] = 0$ and, when $P_T < |k_{\mu F} - k| < k_{\mu F} + k$, it must belong to the interval $[0, \omega_0(P)]$. When $|k_{\mu F} - k| < P_T < k_{\mu F} + k$ instead, $\omega_T(P)$ belongs to the interval $(-\infty, \omega_0(P)]$. If $k_{\mu F} + k < P_T$, then $\omega_T(P) \in (-\infty, 0]$.

- $k_{\mu F} > k$

The expression for $\Sigma_B^R(\mathbf{k}, \omega)^I$ is in this case:

$$\begin{aligned} \Sigma_B^R(\mathbf{k}, \omega)^I &= \frac{1}{(2\pi)^3 k} \int_0^{k_{\mu F}-k} dPP \left\{ \pi [\ln |\rho_B^{II}| + i\pi \Theta(-\rho_B^{II})]_{\omega'=\omega_T(P)} \right. \\ &\times \left. \left| \frac{\partial \text{Re}[T^R(\mathbf{P}, \omega')^{-1}]}{\partial \omega'} \right|_{\omega'=\omega_T(P)}^{-1} + \int_{\omega_0(P)}^{\infty} d\omega' \text{Im} T^R(\mathbf{P}, \omega) [\ln |\rho_B^{II}| - i\pi \Theta(-\rho_B^{II})] \right\} \\ &+ \frac{1}{(2\pi)^3 k} \int_{|k_{\mu F}-k|}^{k_{\mu F}+k} dPP \left\{ \pi [\ln |\rho_B^I| + i\pi \Theta(-\rho_B^I)]_{\omega'=\omega_T(P)} \right. \\ &\times \left. \left| \frac{\partial \text{Re}[T^R(\mathbf{P}, \omega')^{-1}]}{\partial \omega'} \right|_{\omega'=\omega_T(P)}^{-1} + \int_{\omega_0(P)}^{\infty} d\omega' \text{Im} T^R(\mathbf{P}, \omega) [\ln |\rho_B^I| - i\pi \Theta(-\rho_B^I)] \right\} \end{aligned}$$

$$\times \left\{ \left. \frac{\partial \text{Re}[T^R(\mathbf{P}, \omega')^{-1}]}{\partial \omega'} \right|_{\omega'=\omega_T(P)}^{-1} + \int_{\omega_0(P)}^{\infty} d\omega' \text{Im}T^R(\mathbf{P}, \omega) [\ln|\rho_B^I| + i\pi\Theta(-\rho_B^I)] \right\} \quad (2.56)$$

2.8 Momentum distribution functions

In this section we deal with the momentum distribution functions and consider the coherent and incoherent contributions to them; in order to do so, we take into account the poles of the spectral weight functions. In particular, let us call $\omega_F(k)$ and $\omega_B(k)$ the frequencies of the peaks of the fermionic and bosonic spectral weight functions, respectively, that are the solutions of the two equations:

$$\omega - \mathbf{k}^2 + \mu_F - \text{Re}\Sigma_F^R(\mathbf{k}, \omega) = 0 \quad (2.57)$$

$$\omega - \frac{\mathbf{k}^2}{m_B} + \mu_F - \text{Re}\Sigma_B^R(\mathbf{k}, \omega) = 0 \quad (2.58)$$

Equations (2.57) and (2.58) can be understood if we consider Eq. (2.26) after writing explicitly the dressed fermionic and bosonic retarded Green's functions, which leads to:

$$A_F(\mathbf{k}, \omega) = - \frac{\text{Im}\Sigma_F^R(\mathbf{k}, \omega)}{[\omega - \mathbf{k}^2 + \mu_F - \text{Re}\Sigma_F^R(\mathbf{k}, \omega)]^2 + \text{Im}\Sigma_F^R(\mathbf{k}, \omega)^2} \quad (2.59)$$

and to:

$$A_B(\mathbf{k}, \omega) = - \frac{\text{Im}\Sigma_B^R(\mathbf{k}, \omega)}{[\omega - \frac{\mathbf{k}^2}{m_B} + \mu_B - \text{Re}\Sigma_B^R(\mathbf{k}, \omega)]^2 + \text{Im}\Sigma_B^R(\mathbf{k}, \omega)^2} \quad (2.60)$$

A direct inspection of Eqs. (2.59) and (2.60) suggests that, if the imaginary part of the retarded self-energy is zero, then the spectral weight functions can have delta-like contributions. The latter represent quasi-particle excitations with an infinite lifetime. If instead the imaginary part of the retarded self-energy is different from

zero, then quasi-particles acquire a finite lifetime or a fully incoherent spectral function occurs. Having pointed out these aspects, the contributions of the poles to the momentum distributions functions are:

$$n_F^{pol}(\mathbf{k}) = \left| \frac{\partial \text{Re} G_F^{-1}(\mathbf{k}, \omega)}{\partial \omega} \right|_{\omega_{pA_F}}^{-1} \quad (2.61)$$

and:

$$n_B^{pol}(\mathbf{k}) = - \left| \frac{\partial \text{Re} G_B^{-1}(\mathbf{k}, \omega)}{\partial \omega} \right|_{\omega_{pA_B}}^{-1} \quad (2.62)$$

The non-polar contributions to the momentum distribution functions are instead given by:

$$\begin{aligned} n_F^{non-pol}(\mathbf{k}) &= \int_D d\omega A_F(\mathbf{k}, \omega) = \\ &= -\frac{1}{\pi} \int_D d\omega \frac{\text{Im} \Sigma_F^R(\mathbf{k}, \omega)}{[\omega - \mathbf{k}^2 + \mu_F - \text{Re} \Sigma_F^R(\mathbf{k}, \omega)]^2 + \text{Im} \Sigma_F^R(\mathbf{k}, \omega)^2} \end{aligned} \quad (2.63)$$

and:

$$\begin{aligned} n_B^{non-pol}(\mathbf{k}) &= - \int_D d\omega A_B(\mathbf{k}, \omega) = \\ &= \frac{1}{\pi} \int_D d\omega \frac{\text{Im} \Sigma_B^R(\mathbf{k}, \omega)}{[\omega - \frac{\mathbf{k}^2}{m_B} + \mu_B - \text{Re} \Sigma_B^R(\mathbf{k}, \omega)]^2 + \text{Im} \Sigma_B^R(\mathbf{k}, \omega)^2} \end{aligned} \quad (2.64)$$

where $D = \mathbb{R}^- - \{\omega_F(k)\}$ in the fermionic case and $D = \mathbb{R}^- - \{\omega_B(k)\}$ in the bosonic one.

Chapter 3

Building the program

In this Chapter we focus on the aspects which are behind the program for the numerical calculation of the spectral weight functions. Written in *FORTRAN 90* programming language, it is given as inputs some *a priori* known values (e.g. the coupling parameter, the fermionic chemical potential, the bosonic chemical potential, the fraction of the condensate, etc.) and produces several outputs with the primary aim of the determination of the spectral weight functions, as already stated. The input values of the chemical potentials and condensate fraction for given coupling and densities were obtained from previous calculations by Andrea Guidini (University of Camerino) and Christian Gualerzi (University of Bologna). Starting from the T -matrix in the normal and in the condensed phase, whose expressions were derived in Chapter 2, we made use of the integrals reported in section 2.7 in order to compute the fermionic and bosonic self energies; then, knowing these quantities and the bare Green's functions, we used the Dyson's equation to get the spectral weight functions. Some checks have been carried out to verify that the numerical calculation proceeds correctly without errors.

3.1 Adimensionalization of physical quantities

Before writing the code, it is worth considering the dimensionless counterpart of the expressions and relations derived in Chapter 1. In order to do that, let us consider, as a trivial example, the first term of the (2.7), whose dimensional version

is:

$$\Gamma^{\text{SC}}(\mathbf{P}, \Omega)^{-1} = \frac{m_r}{2\pi a_{BF}} - \dots \quad (3.1)$$

A direct inspection of the (3.1) suggests that the dimension of the inverse of the T -matrix in the normal phase in the strong-coupling limit is a mass (m_r) divided by a length (a_{BF}). Therefore, if we want to make dimensionless the previous expression, we have to multiply it for a length and divide it for a mass. Dimensionally speaking, the length is the inverse of the momentum, therefore we can use the Fermi momentum k_F . In systems in which fermions are the majority species, it is customary to set the mass of the fermionic particles m_F as the reference value, i.e. equal to 1. We add a factor 1/2 for the simple reason that several quantities will have a more manageable form in the following. All in all, the dimensionless version of the (3.1) turns out to be:

$$\bar{\Gamma}^{\text{SC}}(\mathbf{P}, \Omega)^{-1} = \frac{m_r}{4\pi m_F k_F a_{BF}} - \dots \quad (3.2)$$

where the - symbol above Γ signals the dimensionlessness. In Eq. (3.2) we recognize in the denominator the inverse of the coupling parameter g , therefore:

$$\bar{\Gamma}^{\text{SC}}(\mathbf{P}, \Omega)^{-1} = \frac{m_r g}{4\pi m_F} - \dots \quad (3.3)$$

Completely analogous reasoning can be quite easily extended to all expressions and relations written in Chapter 2. Notice anyway that the integrals for the bosonic and the fermionic self-energies in section 2.7 are already in their dimensionless form for convenience's sake. From the very beginning, all quantities that appear in the code are appropriately adimensionalized: to sum up, lengths, momenta and masses, as already stated, are measured in units of $\frac{1}{k_F}$, k_F and m_F , respectively, while energies are naturally expressed in units of the Fermi energy E_F .

3.2 The code

The present section is devoted to the aspects behind the implementation of the code in *FORTRAN 90*. The code itself is organized in *subprograms* and *modules*: the former are *functions* and *subroutines* which are quite similar to mathematical functions: they receive a set of input arguments and basically return a value of some type; in this sense, a subroutine can return two or more values or even zero, so it is often regarded as a sort of generalization of a function. A module instead is a package where functions and subroutines can be stored. Typically, it is customary to introduce a module when the program needs to be organically structured because of its size or when functions and subroutines have to be used in more than one program. Throughout the program we worked in *double-precision*. by referring to it, we mean a type of floating-point number which is more precise than a single-precision number. Quantitatively speaking, twice as many bits as a regular floating-point number are used. For clarity's sake, let us consider an example: if a single-precision number requires 32 bits, its double-precision version will need 64 bits. It is important to point to point out that the additional bits raise the precision as well as the range of representable magnitudes and their increment depends on which format the program is using to represent floating-point values.

3.2.1 *T*-matrices, poles and dispersions

At the beginning of the program we defined in a module a series of functions with the aim of building the *T*-matrix for the normal and the condensed phase. From the simplest expressions and moving to the most elaborate ones, we implemented a cascade system of building blocks in which each function - apart the very first ones - contains a function already defined and structured previously. In doing so, we used the expressions derived in section 2.2 (and properly made dimensionless according to the considerations made in section 3.1), taking into account all prescriptions illustrated there. For instance, we defined two functions which are nothing but Eq. (2.7) and its inverse; and so on, covering all relations. While doing that, a retarded counterpart of each function has been built. This means that we performed the analytic continuation of physical quantities from the frequency

imaginary axis to the real one via the replacement $i\Omega \rightarrow \tilde{\Omega} + i0^+$. In *FORTTRAN 90* an operation like that is accomplished via the double complex conversion function $DCMPLX(X, [Y])$: it returns a double complex number where X is converted to the real component; if Y is present it is converted to the imaginary component (if instead it is not so, then the imaginary component is set to 0.0; if X is complex, Y must not be present). In the non retarded version, the second argument is the frequency Ω since it is imaginary, while the action of the analytic continuation leads to a shift of the frequency to the first argument, while the second is now represented by 0^+ ; for the latter we typically used in the program the value 10^{-6} but this has been sometimes changed to larger values in order to better observe the peaks of the retarded T -matrix in the normal and in the condensed phase (times a factor $2m_F k_F$ to ensure dimensionlessness) as a function of the frequency Ω (in units of the Fermi energy). We will discuss these curves and profiles in Chapter 4. The next step is the search for poles of the T -matrix whose importance has already been pointed out in Chapter 2. One of the most reliable procedure is the bisection method that has been extensively used in the program. Recall that the equation that has to be solved when looking for poles is Eq. (2.38):

$$\text{Re}T^R(\mathbf{P}, \Omega(P))^{-1} = 0 \quad (3.4)$$

Preliminarily, we wish to determine the Fermi momentum PT^0 , defined by the above equation, so, basically, we want to solve the following one via the bisection method:

$$\text{Re}T^R(\mathbf{P}, \Omega = 0)^{-1} = 0 \quad (3.5)$$

However, Eq.(3.5) has a divergence for momentum $P = k_{\mu F}$, where $k_{\mu F} = \sqrt{2m_F \mu_F}$ (the dimensionless version, which is the one effectively used, reads: $k_{\mu F} = \sqrt{\mu_F}$). Because of this divergence, the bisection method has to be implemented wisely because the function under consideration is no longer continuous throughout the entire interval. We discriminate between the solutions $P_{T1}^0 > k_{\mu F}$ and $P_{T2}^0 < k_{\mu F}$ by setting proper values of momentum P as extremes of the starting interval and avoiding the divergence located at $k_{\mu F}$ that leads to the loss of the continuity of the function. The position of the poles clearly varies with different values of the coupling parameter g ; results will be discussed in Chapter 3.

The following step in the program is crucial and it involves the calculation of the dispersion relations. Let us start by observing that Eqs. (2.26), (2.15) and (2.16) allow us to affirm, roughly speaking, that the imaginary part of the retarded T -matrix is substantially the spectral function of composite fermions, i.e. molecules composed by one boson and one fermion. When considering the condensed phase of a Bose-Fermi mixture there are δ -like peaks that correspond to the propagation of molecules as well as to the undamped motion of a fermion and a boson. These contributions are due to the poles of the T -matrix and have the dispersions of free particles. A distinction is made between $\Omega_{T1}(P) = P^2/m^* - \mu^*$ that considers the propagation of a fermion and a boson and $\Omega_{T2}(P) = P^2/M^* - \mu'^*$ which takes into account the propagation of a molecule. m^*, M^*, μ^* and μ'^* are parameters which have been determined by a fit procedure that will be discussed in a while. Clearly, compromises between accuracy and computational effort have been made throughout the entire code. Also in the case of dispersions we used the bisection method to solve the following equation:

$$\text{Re}T^R(P = \text{const.}, \Omega)^{-1} = 0 \quad (3.6)$$

Equation (3.6) is nothing but Eq. (3.5) with the difference that now the momentum P is fixed while the variable is the frequency Ω . Since, as explained before, a fit procedure is needed in order to determine the fitting parameters that are contained in the dispersion relations, we have to choose a certain number of points corresponding to different values of the momentum P . To do that, we use *a priori* the subroutine devoted to Gauss-Legendre integration - whose details have been provided in Appendix C - in order to determine a grid of momenta P with their corresponding weights. The inputs are the extremes of integration over momenta P (in units of Fermi momentum k_F) and the number of points with which we sample the interval at issue: as for the former, the inferior extreme is zero while the superior one is given by the pole of the retarded T -matrix already computed at this stage (recall that $\Omega_{T1}(P_{T1}^0) = 0$ and $\Omega_{T2}(P_{T2}^0) = 0$), while, regarding the latter, we decided to sample the interval with 9 points. Since with a real-frequency analysis it can be shown that only the contributions of the retarded T -matrix located at negative frequencies contribute to the self-energies, we did not consider positive frequencies at this stage. We called the subroutine implementing to the

bisection method for every point in the numerical grid for the momentum P leaving the frequency Ω as the variable of the retarded T -matrix. In this way we got 9 different values of the frequency Ω , related to the zero of the retarded T -matrix for the 9 different values of momentum P . Therefore we were able to fit these data with a quadratic function of the type $f(x) = ax^2 + c$ since the dispersion relations have the same form: in particular the inverse of the coefficient a gives the value of the effective masses m^* , M^* , while the effective chemical potentials μ^* and μ'^* are computed via the coefficient c (there is no coefficient b since the dispersion relations do not have a linear term).

3.2.2 Retarded self-energies, spectral weight functions and numerical checks

The core of this subsection is devoted to the implementation in the program of the integrals (2.46) and (2.56) that are directly linked to the fermion and boson self-energies, respectively. Let us now focus on the fermionic case which is the one explored in the present work. The integrand of Eq. (2.46) is built at the code level by simply writing its parts; in particular, there is need to introduce a second variable for the momentum - the external one - and a second variable for the frequency - the external one. The derivative of the real part of the inverse of T^R with respect to the frequency is numerical and it has been implemented by the finite difference method. Regarding the execution of the code up to this point, at the beginning we call the subroutine devoted to the Gauss-Legendre integration and specify a certain number of points to sample the momentum interval, which ranges from 0 to the Fermi momentum P_T^0 of the retarded T -matrix previously determined. The output is the integral of the (2.46) (for chosen values of external momentum and frequency) and in order to get the retarded fermionic self-energy we have to add the remaining parts: in the program there is a specific function that puts all the contributions together. At this stage, knowing the fermionic retarded self-energy and the bare fermionic retarded Green's function, we built the dressed fermionic retarded Green's function via the Dyson's equation. From this we finally obtained the fermionic spectral weight function, according to Eq. (2.26).

Some checks have been carried out. Two main checks, one of which has an important physical meaning, have been implemented: the sum rule (2.30) and the fermionic momentum distribution function (2.32). As for the first, we basically used another time the subroutine with Gauss-Legendre integration; now the integral is performed over the frequency Ω , the extremes of integration are $-\infty$ and $+\infty$ while the integrand is the spectral weight function. We decided to sample the interval with 20,000 points and to use -10 and 10 as extremes of integration: recall in fact that this is a dimensionless quantity - a frequency in units of the Fermi energy E_F . As for the momentum distribution function, similar considerations hold; in this case, however, we had to implement an additional second loop which takes into account the sampling with the external momentum (180 points, from 0.0 to $3.0 k/k_F$).

Chapter 4

Numerical results and analysis

In this Chapter we present the main numerical results obtained after the execution of the program. Even though the previous formal treatment is valid for generic Bose-Fermi mixtures, with $n_F \neq n_B$ and $m_F \neq m_B$, for lack of time in our numerical calculations we focused on the fully balanced case with $n_F = n_B$ and $m_F = m_B$. For the same reason, we limited our numerical study to just the fermionic component, postponing calculations for the bosonic component and more generic situations to future work.

4.1 Retarded T -matrix

We considered some significant values of the coupling parameter $g = 1/k_F a_{BF}$ that allows us to explore the weak, the moderate and the strong-coupling regime. Starting from the definition of Fermi momentum that we gave in section 2.1, we proceeded with the adimensionalization of all the quantities involved.

4.1.1 Retarded Γ -matrix

In this subsection we focus on the behaviour of the retarded Γ -matrix; its imaginary part presents one pole, called $\Omega_T(P_T^0)$, which contributes to the fermionic self-energy only above a certain value of the coupling parameter. Here are the main results concerning (minus) the imaginary part of the retarded Γ -matrix for a concentration $x = n_B/n_F$ value equal to 1 (so $n_F = n_B$) and for a boson-boson

repulsion $\zeta = k_F a_{BB}$ value equal to 0. In Figure 4.1 one can see the appearance of a characteristic peak from the continuum for a momentum $P = 0$ in the weak-coupling region. This peak signals the molecular binding between bosons and fermions, at least "virtually", since in this case is at the edge of the continuum, but not fully separated from it. We observe instead that for larger values of momenta, the peak is fully embedded in the continuum and an increase in the momentum will result in a shift to larger frequencies.

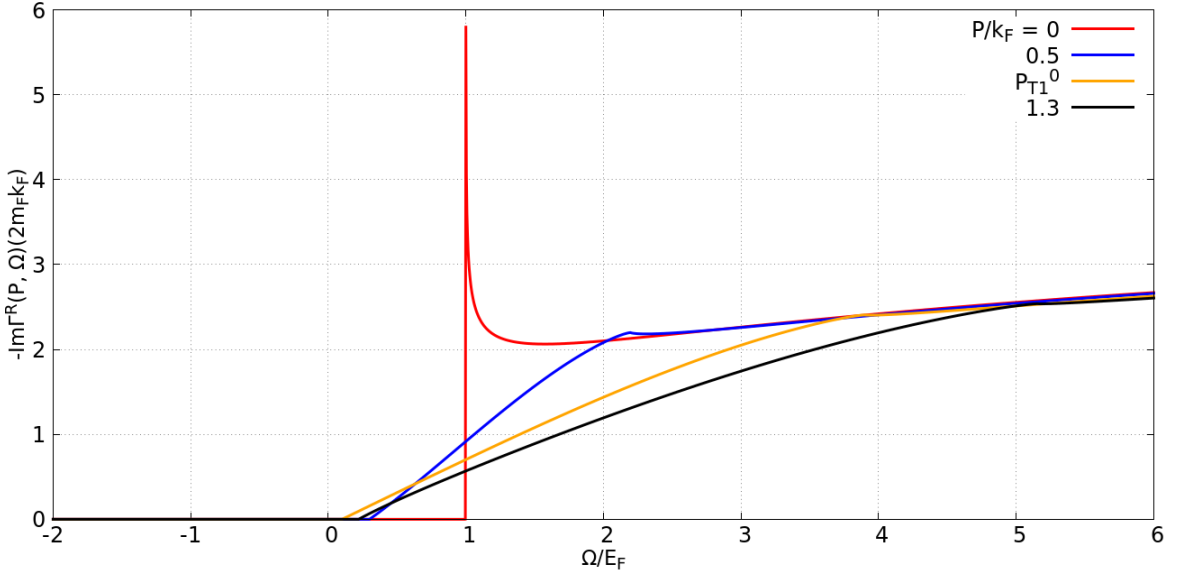


FIGURE 4.1: Minus the imaginary part of $\Gamma^R(\mathbf{P}, \Omega)$ as a function of the frequency Ω for different values of the momentum P for a coupling parameter $g = -3.8$ (weak-coupling regime), corresponding to $\mu_F = 0.901$, $\mu_B = -0.097$ and $\frac{n_0}{n_B} = 0.989$.

In the unitarity case (see Figure 4.2), for $P = 0$ a peak fully separated from the continuum emerges, while for larger values of P the peak becomes again embedded in the continuum meaning that the interaction among bosons and fermions is still not strong enough to allow a bound state for all P . Note furthermore that even the isolated peak at $P = 0$ does not contribute to the fermionic momentum

distribution function since is located at positive frequencies. Such a bound state could be detected only by exciting two-particle excitations at finite energy.

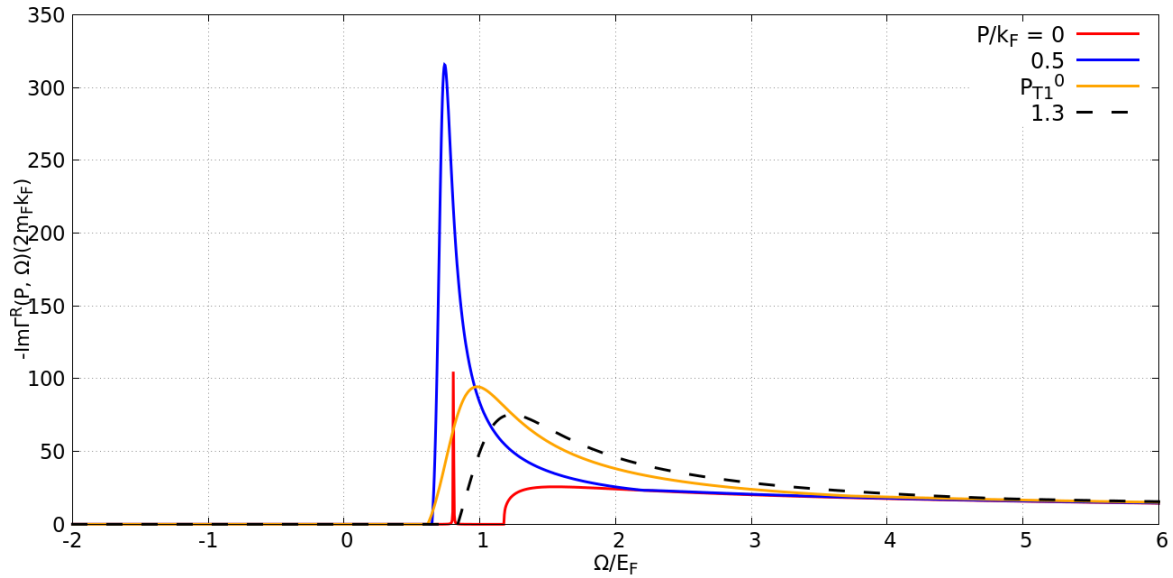


FIGURE 4.2: Minus the imaginary part of the retarded T -matrix $\Gamma^R(\mathbf{P}, \Omega)$ as a function of the frequency Ω for different values of the momentum P for a coupling parameter $g = 0$ (unitarity), corresponding to $\mu_F = 0.611$, $\mu_B = -0.568$ and $\frac{n_0}{n_B} = 0.748$.

In the strong-coupling regime (Figure 4.3) the peak is shifted to negative frequencies, so we are in the presence of a physical bound state that involves one fermion and one boson forming a composite fermion and which contributes to the fermionic momentum distribution function $n_F(k)$. Furthermore, we notice that for a value of momentum P equal to P_Γ^0 the peak is located at zero frequency, as it should be.

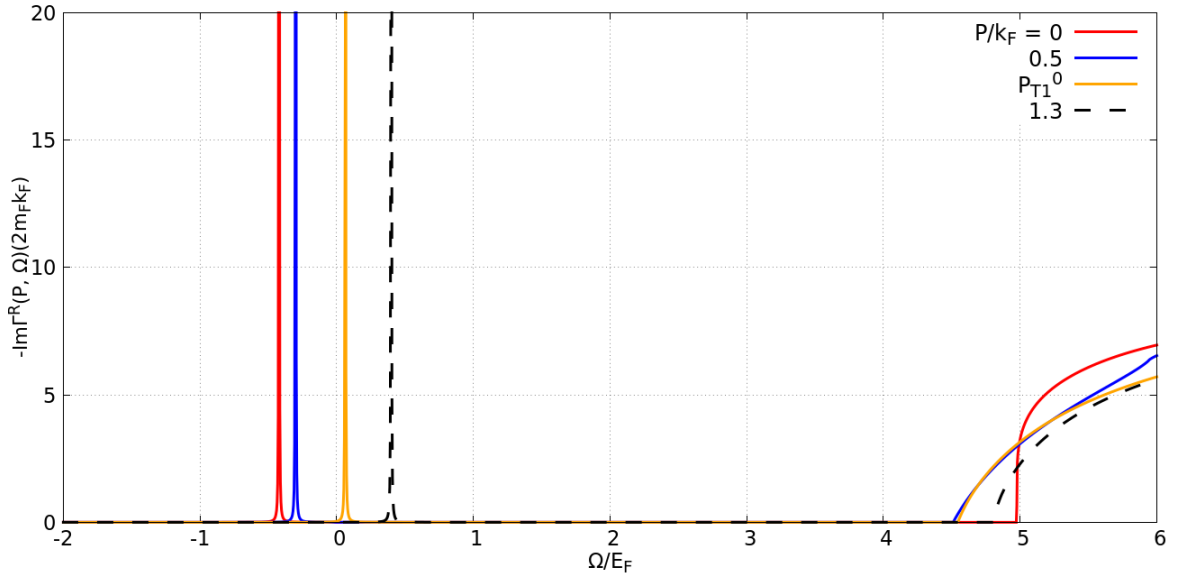


FIGURE 4.3: Minus the imaginary part of the retarded T -matrix $\Gamma^R(\mathbf{P}, \Omega)$ as a function of the frequency Ω for different values of the momentum P for a coupling parameter $g = 1.51$ (strong-coupling), corresponding to $\mu_F = 0.513$, $\mu_B = -4.464$ and $\frac{n_0}{n_B} = 0.025$.

4.1.2 Retarded T -matrix T^R

Let us start with the discussion of the T -matrix T^R for the previous values of coupling parameter g . In the weak-coupling regime, represented in Figure 4.4, we observe two features for all values of P . The feature at larger frequencies is determined essentially by Γ^R and describes pairing correlations. The peak at lower frequencies is associated to the propagation of a free fermion and boson; it is placed at negative frequencies for certain values of the momentum, in particular for all P such that $P < P_{T1}^0$. When instead $P > P_{T1}^0$ (this is the $P = 1.3$ case reported in the graph) this peak is located at positive frequencies; furthermore, it is broadened since it is going to melt with the continuum.

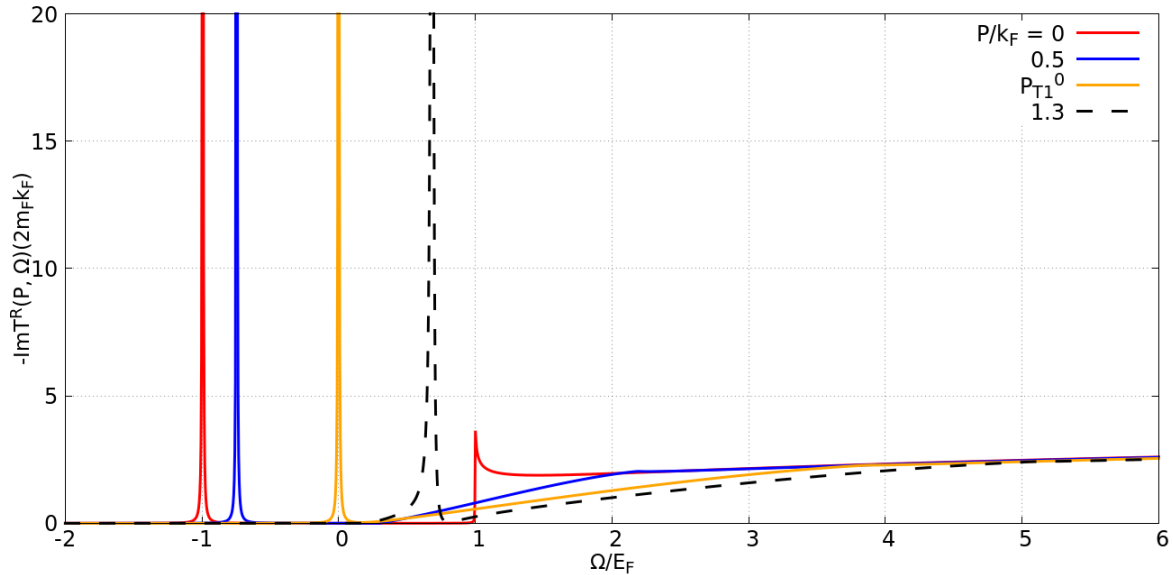


FIGURE 4.4: Minus the imaginary part of the retarded T -matrix $T^R(\mathbf{P}, \Omega)$ as a function of the frequency Ω for different values of the momentum P for a coupling parameter $g = -3.8$ (weak-coupling).

The unitarity regime is shown in Figure 4.5: the considerations made so far with regard to the continuum region and the peaks at lower frequencies continue

to hold.

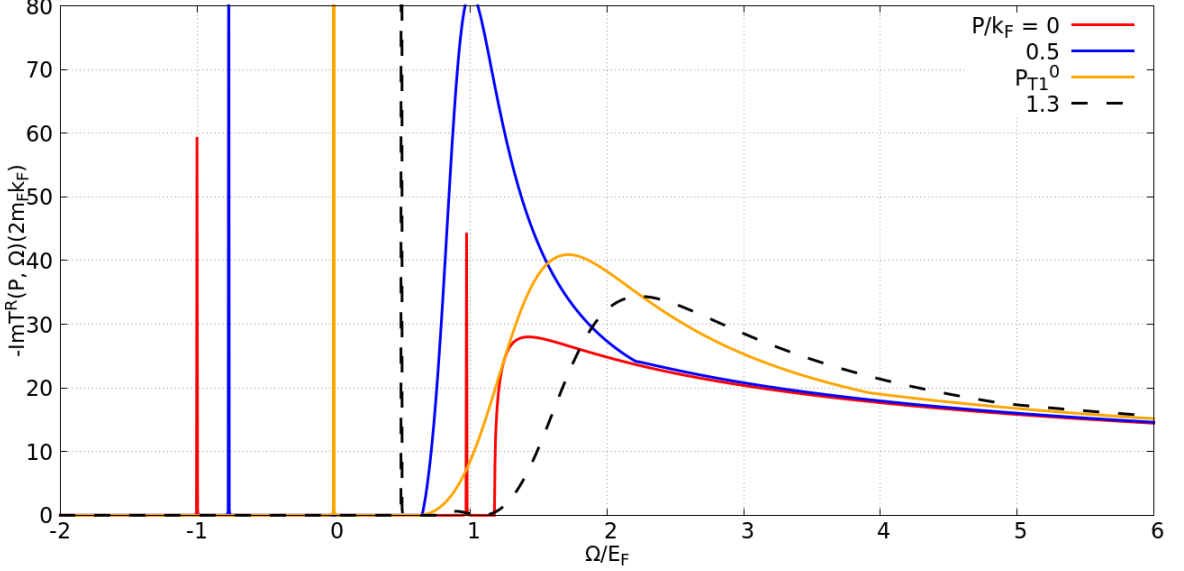


FIGURE 4.5: Minus the imaginary part of the retarded T -matrix $T^R(\mathbf{P}, \Omega)$ as a function of the frequency Ω for different values of the momentum P for a coupling parameter $g = 0$ (unitarity).

In the strong-coupling case (Figure 4.6), one notices first of all the presence of two peaks separated from the continuum for all values of P . Their positions correspond to the two dispersion $\Omega_{T1}(P)$ and $\Omega_{T2}(P)$ mentioned above which will be described in further detail in the next section. These peaks will contribute to the fermionic self-energy only when they are located at negative frequencies. Note finally that for all couplings and momenta the incoherent continuum is located at positive frequencies and will thus not contribute to the fermionic self-energy. All in all, we can make some general considerations when dealing with the retarded T -matrix T^R : an increase in the momentum P will result in a peak shift toward larger values of the frequencies. The propagation of a free particle, be it a fermion or a boson, will have an impact on the self-energies for $0 \leq P \leq P_{T1}^0$. As for the propagation of a molecule, this occurs for sufficiently large values of the

coupling parameter and whenever $0 \leq P \leq P_{T_2}^0$; as a matter of fact, for small values of the coupling parameter, the equation $\Omega_{T_2}(P) = 0$ has no solution and this is reflected in the fact that we observe only peaks located at positive frequencies.

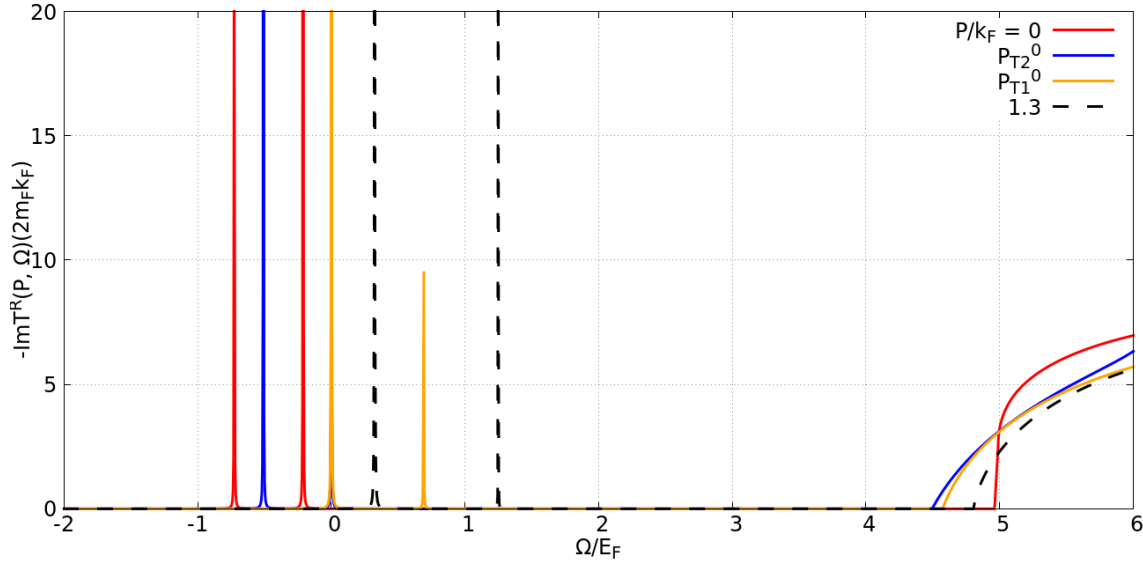


FIGURE 4.6: Minus the imaginary part of the retarded T -matrix $T^R(\mathbf{P}, \Omega)$ as a function of the frequency Ω for different values of the momentum P for a coupling parameter $g=1.51$ (strong-coupling).

4.2 Fermi momentum $P_{\Gamma}^0, P_{T_1}^0, P_{T_2}^0$ and dispersions

In this section we show and discuss the location of the poles of the T -matrix and the profile of the dispersion curves.

As one can see in Figure 4.7, in the weak-coupling regime the interactions between fermions and bosons do not allow the formation of composite fermions: mathematically this is reflected in the features of (minus) the real part of the retarded Γ^R and T^R matrices; as for the former, it has not any divergence and it does not cross

zero (implying that there is no P_Γ^0 momentum), unlike the latter, which displays a divergence at momentum $|\mathbf{P}| = k_{\mu F}$ and it crosses zero at P_{T1}^0 . This different behaviour is explained by means of a direct comparison of Eqs. (2.3) and (2.10). In the unitarity regime, represented in Figure 4.8, identical considerations hold: the coupling is still not enough strong to ensure the existence of P_Γ^0 . Things change significantly when considering the strong-coupling regime (see Figure 4.9): the real part of T^R (for a frequency value Ω set to zero) crosses zero twice, at $P = P_{T2}^0$ and $P = P_{T1}^0$. These two momenta are separated by the divergence placed at $k_{\mu F}$ in such a way that $P = P_{T2}^0 < P < P_{T1}^0$ (clearly we had to take care of this divergence during the application of the bisection method since the function is not continuous everywhere). Furthermore, at $P = P_\Gamma^0$ the real part of the retarded T -matrix in the normal phase (for a frequency value Ω set to zero) crosses zero and this corresponds to the unique possible pole of the retarded Γ -matrix.

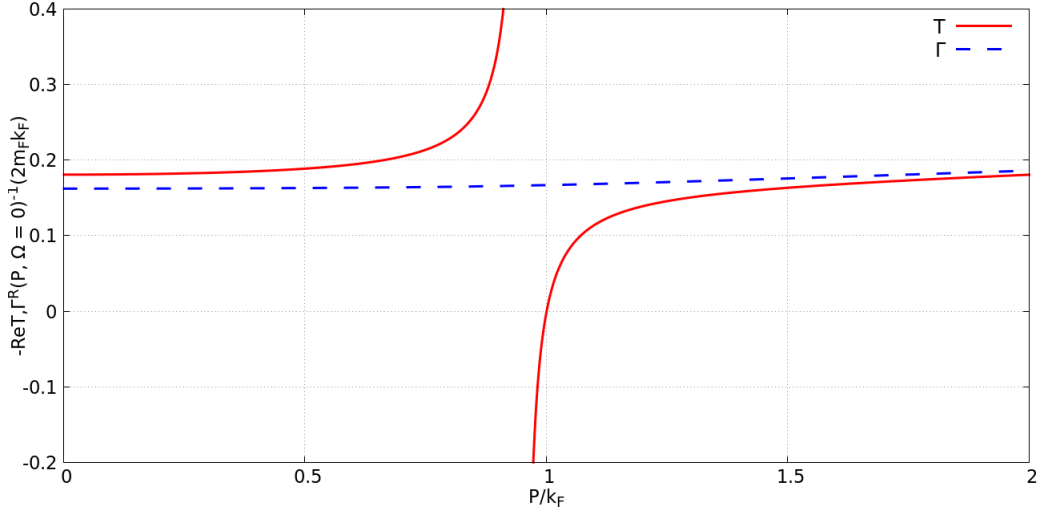


FIGURE 4.7: Minus the real part of $T^R(P, \Omega = 0)^{-1}$ and $\Gamma^R(P, \Omega = 0)^{-1}$ for a coupling parameter $g = -3.8$ (weak-coupling).

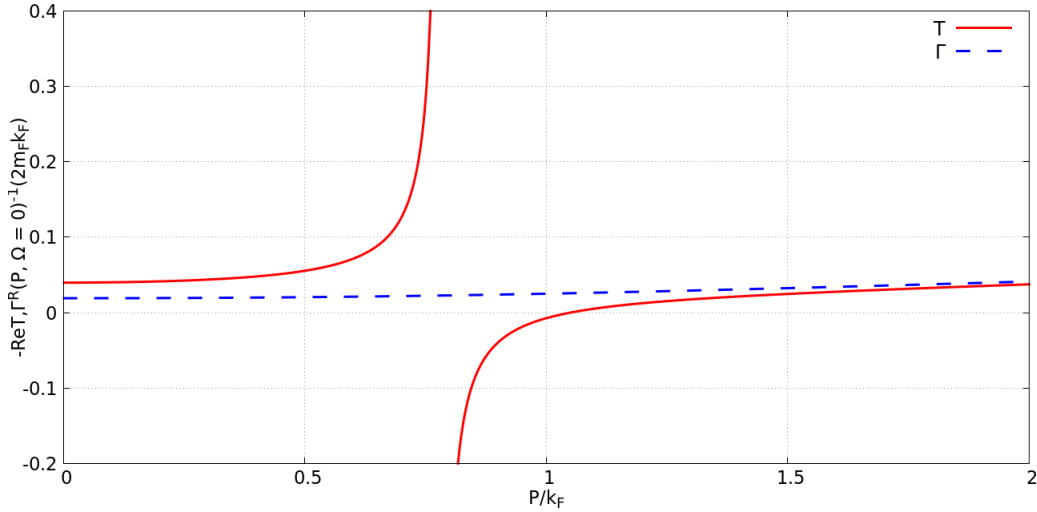


FIGURE 4.8: Minus the real part of $T^R(P, \Omega = 0)^{-1}$ and $\Gamma^R(P, \Omega = 0)^{-1}$ for a coupling parameter $g = 0$ (unitarity).

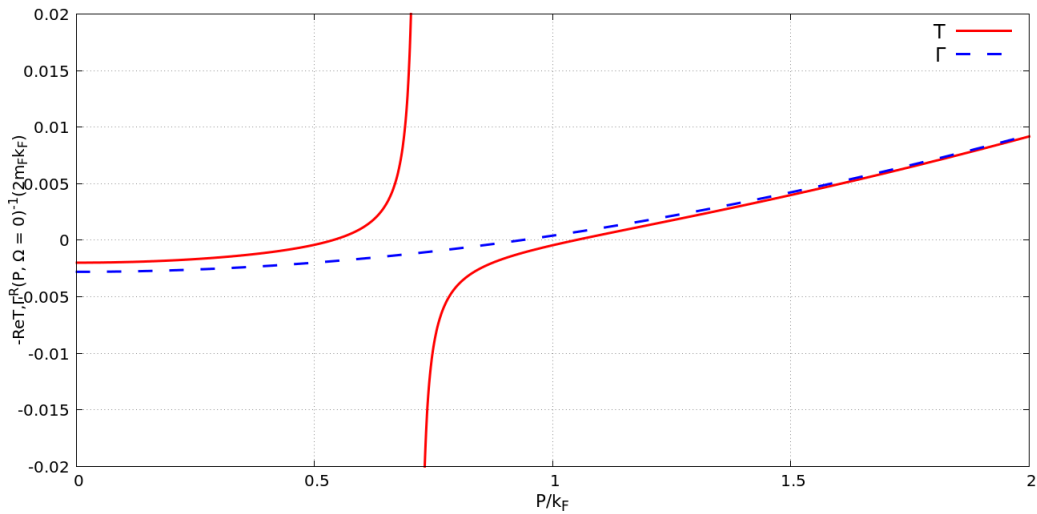


FIGURE 4.9: Minus the real part of $T^R(P, \Omega = 0)^{-1}$ and $\Gamma^R(P, \Omega = 0)^{-1}$ for a coupling parameter $g = 1.51$ (strong-coupling).

Let us now move on the dispersion curves $\Omega_T(P)$. Here are the results for the usual values of the coupling parameter g . In Figure 4.10, we notice that the corresponding dispersion resembles that of a free fermion: the similarity is suggested by the value of the fitting parameters m^* and μ^* which almost coincide with the fermionic mass and the Fermi energy (recall that we are at $T = 0$), respectively. Since the molecular peak in the weak-coupling region is embed in the continuum, as already shown in section 4.1, the dispersion $\Omega_{T2}(P)$ is present. Similar considerations can be made with regard to the unitarity case (see Figure 4.11). Here, the dispersion curve $\Omega_{T2}(P)$ appears only at large positive frequencies meaning that there is no contribution to Σ_F^R . The situation is different when considering the strong-coupling regime (see Figure 4.12) since in this case both dispersions cross zero and thus contribute to the final density of the gas. Regarding the dispersion of the pole of Γ^R instead, we observe that for sufficiently large values of the coupling parameter g the dispersion crosses zero, as already stated. Let us conclude this section with the table 4.1 that sums up the values of the fitting parameters.

Fitting parameters				
Coupling	m^*	μ^*	M^*	μ'^*
-3.80	1.00704 ± 0.00029	-0.994680 ± 0.00028	/	/
0.00	1.13343 ± 0.00984	-0.98866 ± 0.00763	0.62104 ± 0.00992	0.90827 ± 0.02564
1.51	1.611622 ± 0.03343	-0.70497 ± 0.01283	1.14469 ± 0.02315	-0.24624 ± 0.01761

TABLE 4.1: Fitting parameters and asymptotic standard errors calculated with a quadratic fit of the type $f(x) = ax^2 + c$, where a is the inverse of the effective mass(es) and c is the effective chemical potential(s).

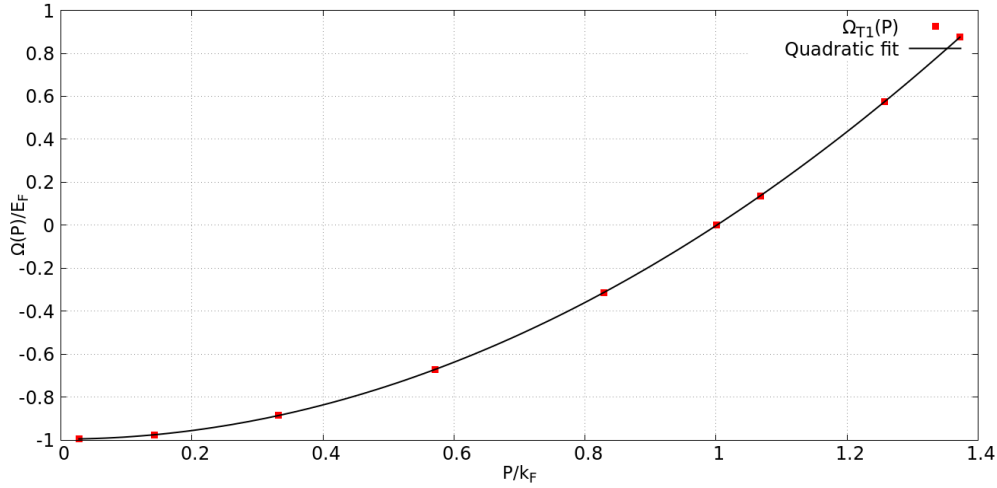


FIGURE 4.10: Dispersion curve obtained after the fitting procedure with a quadratic function for a coupling parameter $g = -3.8$ (weak-coupling).

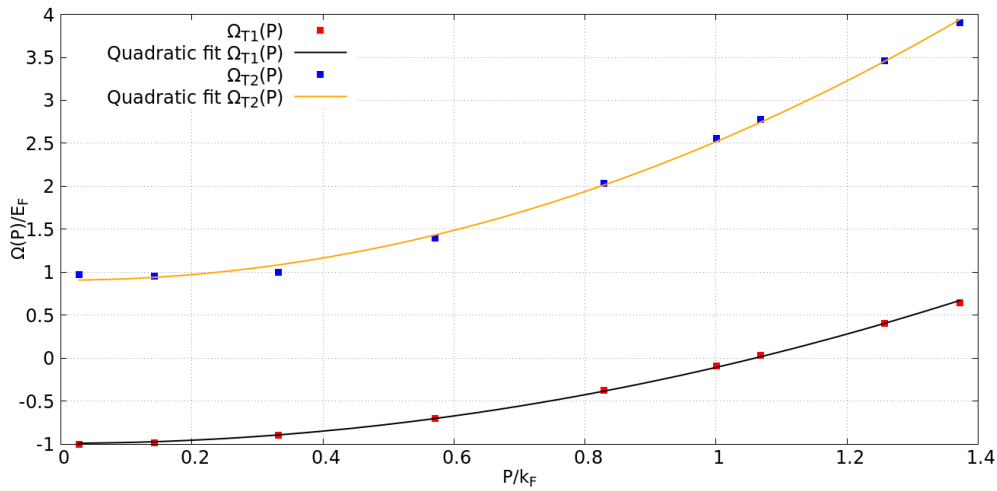


FIGURE 4.11: Dispersion curves obtained after the fitting procedure with a quadratic function for a coupling parameter $g = 0$ (unitarity).

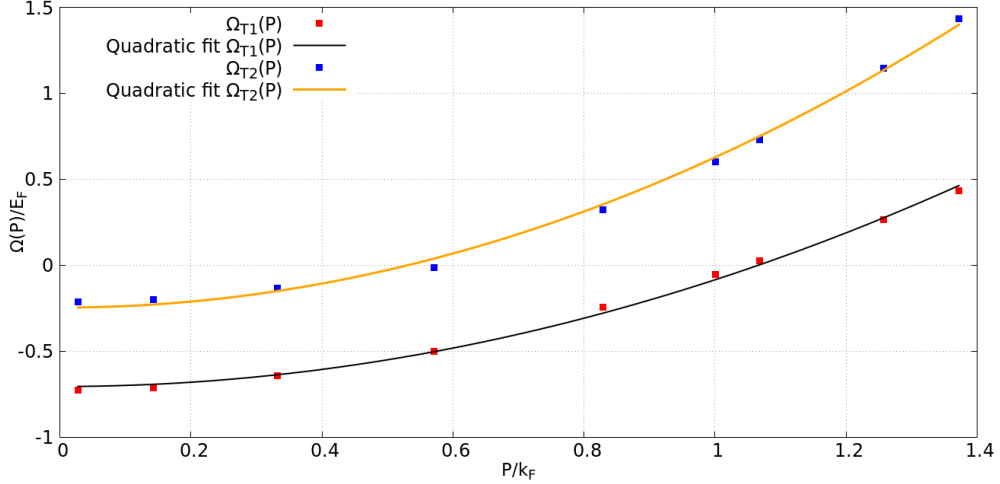


FIGURE 4.12: Dispersion curves obtained after the fitting procedure with a quadratic function for a coupling parameter $g = 1.51$ (strong-coupling).

4.3 Spectral weight functions

This section is entirely devoted to the discussion of the fermionic spectral weight functions for the same values of the coupling parameter g considered above. Here, far from being exhaustive, we report some of the curves and the profiles of the spectral weight functions that we obtained with our numerical calculations and we discuss their main features.

Figure 4.13 shows the profile of $A_F(k, \omega)$ as a function of ω for different values of the momentum k in the weak-coupling regime. In this case we observe a behaviour which is in agreement with that of a Fermi liquid. Very generally speaking, an increase in the momentum will correspond to a peak placed at higher frequencies but there are further considerations that have to be made: first of all, notice that the δ -like peak that is observed for a value of momentum k equal to k_{F1} is located exactly at $\omega = 0$ acting as a watershed between negative frequencies whose corresponding peaks and relative background contribute to the fermionic

momentum distribution function, and positive ones, which do not contribute to $n_F(k)$, but describe the dispersion of single-particle excitations created by adding a fermion to the system. Looking at the former, an increase in the momentum determines a reduction in the width of the peaks (except for the very low momenta case) that assume a δ -like shape until we reach k_{F1} . As stated before, while a δ -like peak represents the propagation of a free particle (in this case, a fermion), a broadened one represents the excitation of a fermion belonging to a molecular state (a composite fermion). A very low value of momentum (a hundredth of k or even smaller) will result in two δ -like peaks (in Figure 4.13 one can see that the second peak in question is significantly flattened even for slightly larger values of the momentum). With regard to the positive frequencies instead, if we increase the momentum k the corresponding peaks become more and more broadened and are shifted towards larger frequencies. All in all, there is a specular situation in the profiles obtained in which the role of the mirror is played by the δ -like peak at k_{F1} . Although we are in the weak-coupling regime and bosons and fermions are supposed to interact only weakly, there is, at least theoretically, a tiny region of small values of momenta (look at the broadened peaks at negative frequencies) in which it seems that some kind of pairing correlations between the two species take place.

Moving to the unitarity regime, shown in Figure 4.14, we observe a different behaviour even if some considerations made previously still hold. First of all, rather surprisingly, all features of the spectral functions are more narrow and δ -like compared to the weaker coupling case. Secondly, we notice the presence of three peaks for low values of the momentum (at $k = 0.05$ and also smaller or slightly larger of the momentum k). The first one, being placed at positive frequencies, describes the behaviour of the system when a fermion is injected into it; this new fermion will remain unpaired and thus, not being able to interact with other particles, it will propagate in the medium (recall that we are considering a perfectly balanced mixture). The other two peaks are found at negative frequencies. Typically, the unique feature that should emerge at negative frequencies stands for the extraction of one fermion from the system. Here, however, we observed an anomalous splitting of this feature that has produced two different branches, one of which represents a molecular state. We speculate that this anomalous structure

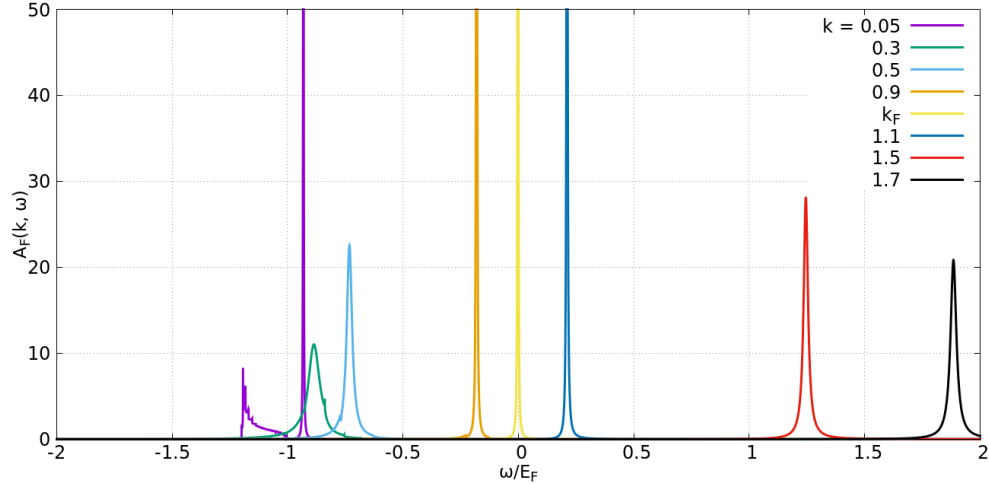


FIGURE 4.13: Curves of the fermionic spectral weight function versus the frequency ω for a coupling parameter $g = -3.8$ (weak-coupling) and different values of the momentum k .

could be connected to the experimental BEC branch observed in [20](#) and whose existence has been not theoretically explained so far, since at unitarity the interaction between bosons and fermions is already quite strong but, meanwhile, the fraction of the condensate is still consistent.

Figure [4.15](#) finally displays a characteristic feature of the fermionic spectral weight functions in the strong-coupling regime, namely the presence of two peaks for each value of the momentum k . In particular, the first peak, which corresponds to lower frequencies, is a δ -like peak, while the second one, placed at higher frequencies, is broadened. Furthermore, the greater the value of the momentum k , the greater the relative distance, in terms of frequencies, of the two peaks.

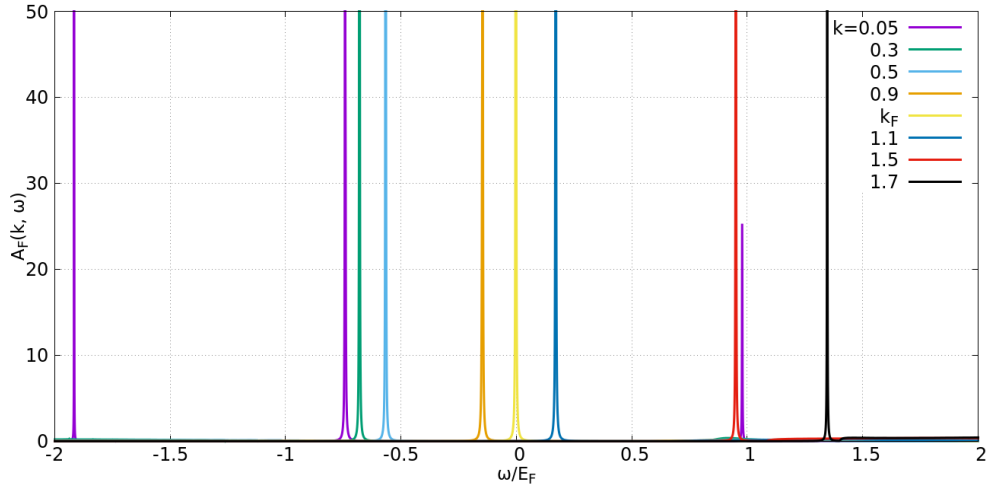


FIGURE 4.14: Curves of the fermionic spectral weight function versus the frequency ω for a coupling parameter $g = 0$ (unitarity) and different values of the momentum k .

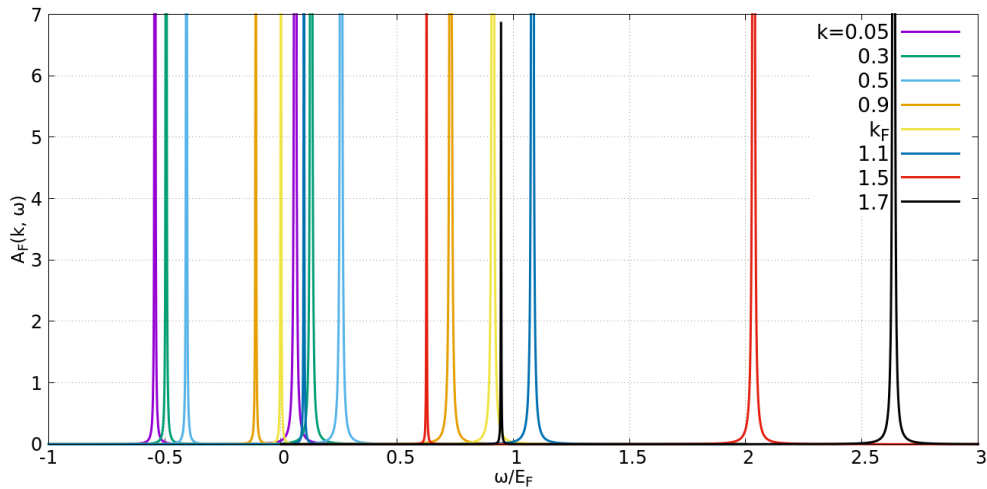


FIGURE 4.15: Curves of the fermionic spectral weight function versus the frequency ω for a coupling parameter $g = 1.51$ (strong-coupling) and different values of the momentum k .

4.4 Numerical checks

Now we show some results that can validate the profiles of the spectral weight functions. We already discussed in section 3.2.2 the importance and the need of these type of checks: they are not ends in themselves but have a deep physical meaning.

4.4.1 Sum rule

Equation (2.30) is a condition that all spectral weight functions must verify. This relation has been checked for the coupling parameters considered so far and the results obtained are, within the limits of the accuracy of the calculator, satisfactory since they are within 1% tolerance. Here we just want to make an observation: since the integral over the frequencies ω has to be performed between $-\infty$ and ∞ , one may mistakenly think that, with the same number of points, the sampling of a bigger interval will provide a better value of the integral, certainly closer to 1. Actually this is not true because, doing so, δ -like peaks in the spectrum are not properly sampled with an adequately high number of points and therefore their contribution, which is very significant, is not correctly recovered.

4.4.2 Fermionic momentum distribution function

The fermionic momentum distribution function $n_F(\mathbf{k})$ can be regarded as an important check and represents by itself an interesting physical object. Equation (2.32) has been implemented in the code and here are the results for a balanced Bose-Fermi mixtures with equal masses and for the values of the coupling parameter considered so far. In Figure 4.16 we can notice that in the weak-coupling regime (red line) the fermionic momentum distribution is essentially that of a Fermi gas with the characteristic sudden jump at k_F which represents the step. According to Luttinger's theorem [51], fermions behave as a Fermi liquid, therefore the occupancy decreases progressively before the step. If we consider higher couplings, i.e. 0 and 1.51, the value of $n_F(\mathbf{k})$ before the Fermi step is significantly

smaller and its decrease more pronounced: this is an effect of the interactions that, becoming stronger, reduce the number of unpaired fermions belonging to the Fermi sphere and make them interact more intensely with bosons. As a result, for high momenta we expect that the fermionic momentum distribution function should have greater values after the Fermi step and this behaviour is clearly recovered: see the tails of the curves that become larger when the coupling parameter is increased. In Figure 4.16 we also report as an important numerical check the momentum distribution function as calculated previously in a completely independent way without integrating the spectral weight function but working instead only with imaginary frequencies. The results obtained by the two methods match very well.

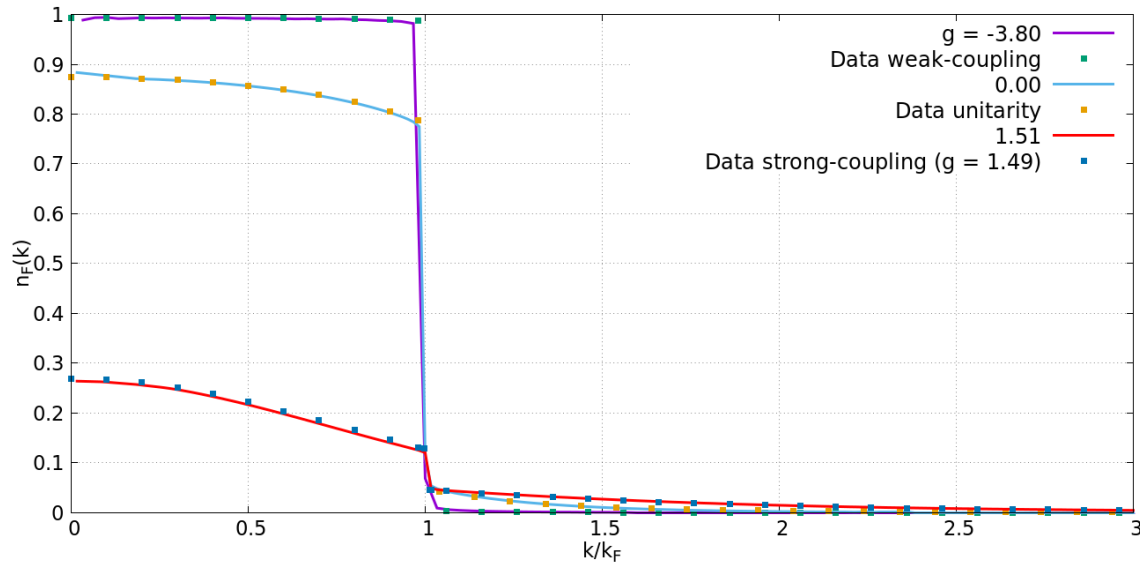


FIGURE 4.16: Fermionic momentum distribution function $n_F(k)$ versus the momentum k for different values of the coupling parameter: -3.8 (weak-coupling), 0 (unitarity) and 1.51 (strong-coupling).

As for the magnitude of the jumps of the curves of the distributions, which are sudden in weak-coupling regimes and smoother in strong ones, we will make

some considerations with regard to the quasi-particle residue in the following, since it represents the height of the Fermi step.

4.4.3 Quasi-particle residue

Figure 4.17 presents the quasi-particle residue $Z(g)$ at the Fermi step k_{F1} of the momentum distribution function for different coupling values. We can observe that the quasi-particle residue is approximately equal to 1 in the weak-coupling regime thus showing the features of an almost non-interacting system. When moving to higher values of the coupling parameter, the quasi-particle residue undergoes a decrease since now, as already pointed out in the previous subsection, the occupancy at momenta smaller than k_F is lowered while the one at momenta higher than k_F increases. For a balanced Bose-Fermi mixture like ours, the quasi-particle residue becomes zero at the critical coupling g_c , that is the highest value of the coupling parameter g (in our case, $g_c \approx 1.61$) at which the condensate fraction vanishes at zero temperature owing to the exclusive formation of bound states. Therefore at g_c we have a quantum phase transition and we assist at the breakdown of the Fermi liquid behaviour. This means, thinking in terms of the fermionic part, that there are no more unpaired fermions.

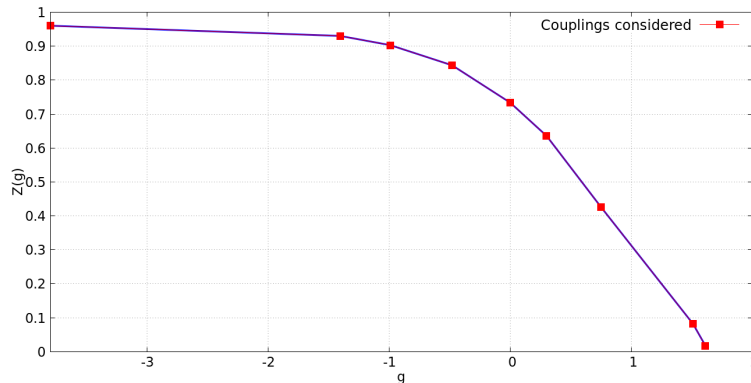


FIGURE 4.17: Quasi-particle residue $Z(g)$ as a function of the coupling parameter g , starting from $g = -3.8$ (weak-coupling) and ending with $g = 1.61$ (which is approximately the critical coupling).

Chapter 5

Outlooks and concluding remarks

In this final Chapter, after setting the basis for a later study, we briefly discuss Bose-Fermi mixtures in the presence of mass and/or density imbalance. So far we have considered systems made of bosons and fermions with equal masses and densities, therefore we want to elaborate a little bit on this more general aspect as well as to take into account systems in which the bosons are the majority species.

5.1 Future perspectives

In our theoretical study in Chapter 2 we dealt with the bosonic and the fermionic parts of the mixtures providing an almost exhaustive scenario with regard to the physical quantities involved and the equations that rule the system, but in the numerical calculations, for time reasons, we decided to focus exclusively on the fermionic component. However, the implementation of the bosonic counterpart involves the determination of the integral of the corresponding self-energy whose details have been given in section 2.7; the calculus is not straightforward since some computational complications arise (recall in fact Eqs. (2.55) and (2.56)) but one, starting from the T -matrices, Γ^R and T^R which are common to bosons and fermions, has to retrace the steps carried out in the fermionic component in order to reach the bosonic spectral weight function and all the consequent physical quantities that have been analyzed in the fermionic case. This will be the object of future study that will lead us to a deeper understanding of mutual interactions between bosons and fermions.

In several previous works the role of mass and density imbalances have been analyzed. For example, in [42], it has been shown that a mass imbalance of the type $m_B/m_F < 1$ determines a dramatic change in the critical coupling g_c making it increase very quickly especially when the mass of the bosons is almost negligible if compared to that of the fermions. These considerations instead does not apply when it comes to the introduction of a density imbalance since the critical coupling g_c is slightly affected in this case. In [52] it has been shown that there is a threshold for the concentration $x = n_B/n_F$, fixed at $x = 0.5$, that can be regarded as a border between two different behaviours of the fermionic (and bosonic) momentum distribution function for strong coupling. In particular the evolution of the jump(s) changes significantly from the case that we focused on: in fact, as the coupling parameter is increased and for $x < 0.5$, k_{F1} reaches k_{UF} while k_{F2} approaches P_{CF} , where $k_{UF} \equiv (6\pi^2 n_{UF})^{1/3}$ and $P_{CF} \equiv (6\pi^2 n_{CF})^{1/3}$, being $n_{UF} = n_F - n_B$ and $n_{CF} = n_B$ the unpaired excess fermions density and the density of molecules, respectively. In general, at the critical coupling the unpaired excess atoms fill the Fermi sphere up to a momentum that reaches k_{UF} in the molecular limit. This implies that the fermionic momentum distribution function passes from weak to strong couplings with a smooth crossover in a range of values of g for which there are two jumps (and, consequently, two quasi-particle residues) at k_{F1} and k_{F2} . As for systems in which bosons are the majority species, recall the considerations made in the introduction with regard to the nature of the interactions which are now attractive. One of the most interesting feature is the behaviour of the quasi-particle residue which, in the strong-coupling regime, vanishes asymptotically: this means that, unlike in the case in which fermions are the majority species and the Bose-Einstein condensation is suppressed at the finite value of the critical coupling g_c (for $x \leq 1$), it is not possible to find a finite value of the coupling parameter at which the totality of fermions are bound to bosons. It would be very interesting to explore the spectral weight functions also in this context.

5.2 Concluding remarks

In this thesis we have studied Bose-Fermi mixtures in the condensed phase by means of Green's functions formalism at zero temperature with Feynman's diagrams computed within the framework of T -matrix approximation. The focus was on fermionic spectral weight functions obtained numerically after a proper manipulation of the integrals involved in the retarded self-energies. The profiles of the quantities that we have obtained - starting from the retarded T -matrix Γ^R and ending with the quasi-particle residue Z - that we have obtained reproduce by and large the expected physical behaviour of the system under consideration. Consider for example the fermionic distribution function and its progressive depletion before the Fermi step, as well as the reduction of the height of its jump as the coupling parameter is increased: this is a consequence of the fact that stronger interactions reduce the number of unpaired fermions that belong to the Fermi sphere making them interact more significantly with bosons. Furthermore, we have shown that the quasi-particle residue becomes zero in correspondence of the critical coupling: there is a quantum phase transition in which the fraction of the condensate vanishes indicating the breakdown of the Fermi liquid behaviour at g_c . However, there are some results, obtained in the unitarity region (where the boson-fermion scattering length diverges), whose interpretation is not totally understood: in the fermionic spectral weight function we have observed that all the features corresponding to the values of the momentum considered are more narrow and δ -like compared to the weaker coupling case; we should have expected more broadened profiles instead, so this aspect deserves further investigations. Moreover, we assisted at the emergence of three peaks for low values of the momentum: the one placed at positive frequencies represents the behaviour of the system when a fermion is injected into it; since we are considering a perfectly balanced mixture, this new fermion will remain unpaired and thus, not being able to interact with other particles, it will propagate in the medium; the two remaining peaks are located at negative frequencies. Typically, the single feature that emerges at negative frequencies, as previously stated, has to be interpreted as the extraction of one fermion from the system. Here, however, we have assisted at an anomalous splitting of this feature that has produced two different branches,

one of which represents a molecular state. We speculate that, since at unitarity the interaction between bosons and fermions is already quite strong but, at the same time, the fraction of the condensate is still consistent, this anomalous structure could be connected to the experimental BEC branch observed in [20] and whose existence has been not theoretically explained so far. The next step will consist in the analysis of the fermionic spectral weight functions for values of the coupling parameter near to that of unitarity in order to make sure of the presence of this double peak structure in a certain interval of interactions and try, if possible, to delimit its domain.

Appendix A

Quasi-particle theory

Like with the propagator of independent particles, a quasi-particle is primarily defined to be a simple pole of the propagator:

$$\omega - \zeta_{\mathbf{k}} - \Sigma^R(\mathbf{k}, \omega) = 0 \quad (\text{A.1})$$

The propagator, with the pole at $\omega_1(\mathbf{k}, \omega) + i\omega_2(\mathbf{k})$, has the form of a quasi-particle propagator and a regular part:

$$G(\mathbf{k}, \omega) = \frac{Z(\mathbf{k})}{\omega - \omega_1(\mathbf{k}) - i\omega_2(\mathbf{k})} + G^{reg}(\mathbf{k}, \omega) \quad (\text{A.2})$$

In Eq. (A.2) the residue $Z(\mathbf{k})$ can be thought as the quasi-particle weight and the sum rule for the spectral functions implies that $Z(\mathbf{k})$ can take only positive values which are not greater than 1, i.e. $0 \leq Z(\mathbf{k}) \leq 1$. Using the Lehmann representation one can show that ω_2 has the sign of $\mu - \hbar\omega_1$. Therefore:

$$iG(\mathbf{k}, t) = iG^{reg}(\mathbf{k}, t) + \begin{cases} Z(\mathbf{k})e^{-i\omega_1(\mathbf{k})t + \omega_2(\mathbf{k})t}\theta(\hbar\omega_1 > \mu) & t > 0 \\ -Z(\mathbf{k})e^{-i\omega_1(\mathbf{k})t + \omega_2(\mathbf{k})t}\theta(\hbar\omega_1 < \mu) & t < 0 \end{cases} \quad (\text{A.3})$$

As a consequence, $\omega_2(\mathbf{k})t < 0$ always describes the damping of the quasi-particle mode. In particular, if the pole is in the vicinity of the real axis, the lifetime can be regarded as long and a frequency integral of the propagator is very enhanced in its neighbourhood with a particle-like contribution that is weighted by the residue.

If we admit that ω_2 is small, the notion of quasi-particle itself is useful. Starting from Eq. (A.1), one gets:

$$\omega_1(\mathbf{k}) - \tilde{\zeta}_{\mathbf{k}} - \text{Re}\Sigma^R(\mathbf{k}, \omega_1(\mathbf{k})) = 0 \quad (\text{A.4})$$

$$\omega_2(\mathbf{k}) = Z(\mathbf{k})\text{Im}\Sigma^R(\mathbf{k}, \omega_1(\mathbf{k})) \quad (\text{A.5})$$

$$Z(\mathbf{k}) = \left| 1 - \frac{\partial}{\partial \omega} \text{Re}\Sigma_F^R(\mathbf{k}, \omega) \right|_{\omega=\omega_1(\mathbf{k})}^{-1} \quad (\text{A.6})$$

Notice that Eqs. (A.4) and (A.6) have also been discussed in section 2.6.

In general, the assumption according to which ω_2 is small is guaranteed by $\hbar\omega_1$ close to the Fermi energy, where the imaginary part of the retarded self-energy is zero. Then we are able to give a quantitative interpretation of the smallness of ω_2 , that is $|\omega_2| \ll |\omega_1 - \mu/\hbar|$. All in all, a quasi-particle is mainly characterized by three properties:

- 1) it is a pole of the propagator in the complex ω plane;
- 2) the residue $Z(\mathbf{k})$ is not negligible, meaning that is of order 1;
- 3) it satisfies the "smallness" condition regarding ω_2 : $|\omega_2| \ll |\omega_1 - \mu/\hbar|$

Now let us show why the presence of a quasi-particle is reflected in a discontinuity in the momentum density across the Fermi surface. The latter is defined as the set of \mathbf{k} vectors such that:

$$\frac{\mu}{\hbar} - \tilde{\zeta}_{\mathbf{k}} - \Sigma^R(\mathbf{k}, \frac{\mu}{\hbar}) = 0 \quad (\text{A.7})$$

We start from:

$$n(\mathbf{k}) = -iG(\mathbf{k}, 0^-) = \int_{-\infty}^{\infty} \frac{d\omega}{2\pi i} G(\mathbf{k}, \omega) e^{i\omega 0^+} \quad (\text{A.8})$$

and then we evaluate the (A.8) with the pole expansion given by the (A.2). The residue theorem provides:

$$n(\mathbf{k}) = n^{reg}(\mathbf{k}) + \begin{cases} Z(\mathbf{k}) & \hbar\omega_1(\mathbf{k}) < \mu \\ 0 & \hbar\omega_1(\mathbf{k}) > \mu \end{cases} \quad (\text{A.9})$$

Equation (A.7), which is the equation defining the Fermi surface, is equivalent to $\hbar\omega_1(\mathbf{k}) = \mu$. At a point \mathbf{k} of the surface the jump turns out to be:

$$n(\mathbf{k}^<) - n(\mathbf{k}^>) = Z(\mathbf{k}) \quad (\text{A.10})$$

Appendix B

Bisection method

The bisection method is based on a root-finding algorithm; this can be applied to any continuous function for which two values with opposite signs are known. The core of the method, as the name itself suggests, is the repeated bisection of the interval defined by these values and the subsequent selection of the subinterval in which the function changes sign and, consequently, must contain a root. Overall, if on one hand is a quite simple and robust method, on the other is relatively slow and for these reasons it is typically used when one wants to get a rough approximation to a solution (the latter is the starting point for more rapidly converging methods). However the bisection method, being suitable for our purposes, has been used extensively in order to find the poles of the T -matrix.

Quantitatively speaking, let f be a continuous function defined on an interval $[a, b]$ such that $f(a)$ and $f(b)$ have opposite signs. Under these assumptions, the intermediate value theorem holds: the continuous function f must have at least one root in the interval (a, b) . The bisection method numerically solves the equation $f(x) = 0$ for the real variable x . At each step, the midpoint $c = (a + b)/2$ of the interval is computed as well as the value of the function $f(c)$. If c itself is a root, then the algorithm has succeeded and ends; if it is not so, there are two possibilities: either $f(a)$ and $f(c)$ or $f(c)$ and $f(b)$ have opposite signs and bracket a root. At this stage, the subinterval that is guaranteed to be a bracket as well as the new interval to be used in the next iteration. By doing this, the interval which contains a zero of f encounters a reduction in width by 50% at each step. The process is repeated until the interval is sufficiently small (that is, $c - a$ is sufficiently small or $|f(c)|$ is sufficiently small) leading to a satisfactory convergence, which is linear

because the absolute error is halved at each iteration. More precisely, if $c_1 = \frac{a+b}{2}$ is the midpoint of the starting interval while c_n is the midpoint of the interval in the n -th step, then the difference between c_n and a solution c turns out to be bounded in the following way: $|c_n - c| \leq \frac{|b-a|}{2^n}$. The previous formula is useful to determine *a priori* an upper bound regarding the number of iterations n that are required by the method to converge to a root with an arbitrary tolerance ϵ (in the program we set $\epsilon = 10^{-7}$). In particular, we have: $n \leq n_{1/2} \equiv \left\lceil \log_2\left(\frac{|b-a|}{\epsilon}\right) \right\rceil$. There are no other methods that can guarantee the production of an estimate c_n to the solution c that in the worst case has an ϵ absolute error with less than $n_{1/2}$ iterations and this is the main reason why the bisection method has proved to be optimal while considering the worst case performance under absolute error criteria.

An important remark is the following: even if f is continuous, finite precision, which is intrinsic to computers, may preclude a function value ever being zero. For instance, this is the case of functions like $f(x) = x - \pi$; we can notice that there will never be a finite representation of x that gives zero. Furthermore, the difference between a and b is technically limited by the floating point precision: this means that if we assist to the decrease of the difference between a and b , at some stage the midpoint of $[a, b]$ will be identical, from a numerical point of view, to either a or b within their floating point precision.

Appendix C

Gauss-Legendre integration

There are many integrals along the dissertation that must be computed numerically. An efficient algorithm to determine integrals of regular functions (i.e. well approximated with a polynomial) with a great accuracy is the Gaussian quadrature method; this was extensively used in our program.

When the integrating function is the product of a polynomial times a certain known function $W(x)$, it is possible to choose the abscissa and the weights such that the integral computed with the quadrature method is exact. In general, let $W(x)$ be a certain known function and N an integer; then, it is possible to find a set of N abscissa x_j and of N weights such that:

$$\int_a^b dx W(x) f(x) \approx \sum_{j=1}^N w_j f(x_j) \quad (\text{C.1})$$

Equation (C.2) admits the equal sign if $f(x)$ is a polynomial of degree N . Typically, given the integrating function $g(x)$, it is useful to choose a proper weight function $W(x)$ so that:

$$\int_a^b dx g(x) \approx \sum_{j=1}^N v_j g(x_j) \quad (\text{C.2})$$

where $g(x) \equiv W(x)f(x)$ and $v_j \equiv \frac{w_j}{W(x_j)}$. The N abscissa which belong to a gaussian quadrature of the type (C.2) are, with a weight function $W(x)$ in an interval

$[a, b]$, the roots of the orthogonal polynomial $p_N(x)$ for the same weight function and the same interval. Recall that, given a weight function $W(x)$ it is possible to determine a set of orthogonal polynomials $p_j(x)$ of degree $j = 0, 1, 2, \dots$, which have scalar products weighted by $W(x)$ equal to zero. Mathematically, $\int_a^b dx W(x) p_j(x) p_i(x) = 0$. The most common set of abscissa and weights is the Gauss-Legendre one: it comes from the weight function $W(x) = 1$, with $-1 < x < 1$, whose orthogonal polynomials are the Legendre polynomials $P_n(x)$. For a generic integration interval $[a, b]$, the following formula allows one to determine the weights:

$$w_j = \frac{2}{(1 - x_j)^2 [P'_N(x)]^2} \quad (\text{C.3})$$

while the integral of a function $f(x)$ is given by:

$$\int_a^b f(x) \approx \sum_{j=1}^N w_j f(x_j) \quad (\text{C.4})$$

The GAULEG subroutine, slightly modified from [53], computes the abscissa and the weights with the Gauss-Legendre method. As inputs we have the extremes of the integration and the number of points N with which to calculate the integral; at this stage, the subroutine looks for the roots of the N -th Legendre polynomial, then computes the weights for each root according to the (C.3). As outputs, we have the N -dimensional vectors of the abscissa and the weights. An important consideration is the following: since the inputs and the outputs do not depend on the integrating function, the same abscissa and weights can be used for every integration if the extremes and the number of points N are kept fixed.

Bibliography

- [1] A. Einstein, Sitzungsberichte der Preussischen Akademie der Wissenschaften, Physikalisch-mathematische Klasse p. 261 (1924); p. 3 (1925).
- [2] S. N. Bose, *Plancks Gesetz und Lichtquantenhypothese*, Zeitschrift für Physik, **26**, pp. 178-181 (1924).
- [3] M. H. Anderson, J. R. Ensher, M. R. Matthews, C. E. Wieman, and E. A. Cornell, Observation of Bose-Einstein Condensation in a Dilute Atomic Vapor, *Science* **269**, 198 (1995).
- [4] K. B. Davis, M. O. Mewes, M. R. Andrews, N. J. van Druten, D. S. Durfee, D. M. Kurn, and W. Ketterle, Bose-Einstein Condensation in a Gas of Sodium Atoms, *Phys. Rev. Lett.* **75**, 3969 (1995).
- [5] L. Viverit, C. J. Pethik, and H. Smith, Influence of Induced Interactions on the Superfluid Transition in Dilute Fermi Gases, *Phys. Rev. A* **61**, 053605 (2000).
- [6] A. P. Albus, S. A. Gardiner, F. Illuminati, and M. Wilkens, Quantum field theory of dilute homogeneous Bose-Fermi mixtures at zero temperature: General formalism and beyond mean-field corrections, *Phys. Rev. A* **65**, 053607 (2002).
- [7] S. Powell, S. Sahdev, and H.P. Buhler, Depletion of the Bose-Einstein condensate in Bose-Fermi mixtures, *Phys. Rev. B* **72**, 024534 (2005).
- [8] D. C. E. Bortolotti, A. V. Avdeenkov, and J. L. Bohn, Generalized mean-field approach to a resonant Bose-Fermi mixture, *Phys. Rev. A* **78**, 063612 (2008).

-
- [9] X. Barillier-Pertuisel, S. Pittel, L. Pollet, and P. Schuck, Boson-fermion pairing in Bose-Fermi mixtures on one-dimensional optical lattices, *Phys. Rev. A* **77**, 012115 (2008).
- [10] I. Titvinidze, M. Snoek, and W. Hofstetter, Generalized dynamical mean-field theory for Bose-Fermi mixtures in optical lattices, *Phys. Rev. B* **79**, 144506 (2009).
- [11] F. M. Marchetti, T. Jolicoeur, and M. M. Parish, Stability and Pairing in Quasi-One-Dimensional Bose-Fermi Mixtures, *Phys. Rev. Lett.* **103**, 105304 (2009).
- [12] T. Watanabe, T. Suzuki, and P. Schuck, Bose-Fermi pair correlations in attractively interacting Bose-Fermi atomic mixtures, *Phys. Rev. A* **78**, 033601 (2008).
- [13] G. Bertaina, E. Fratini, S. Giorgini, and P. Pieri, Quantum Monte Carlo Study of a Resonant Bose-Fermi Mixture, *Phys. Rev. Lett.* **110**, 115303 (2013).
- [14] A. Yamamoto and T. Hatsuda, Quantum Monte Carlo simulation of three-dimensional Bose-Fermi mixtures, *Phys. Rev. A* **86**, 043627 (2012).
- [15] C. H. Wu, J.W. Park, P. Ahmadi, S. Will, and M. W. Zwierlein, Ultracold Fermionic Feshbach Molecules of $^{23}\text{Na}^{40}\text{K}$, *Phys. Rev. Lett.* **109**, 085301 (2012).
- [16] M. S. Heo, T. T. Wang, C. A. Christensen, T. M. Rvachov, D. A. Cotta, J. H. Choi, Y. R. Lee, and W. Ketterle, Formation of ultracold fermionic NaLi Feshbach molecules, *Phys. Rev. A* **86**, 021602(R) (2012).
- [17] T. D. Cumby, R. A. Shewmon, M.-G. Hu, J. D. Perreault, and D. S. Jin, Feshbach molecule formation in a Bose-Fermi mixture, *Phys. Rev. A* **87**, 012703 (2013).
- [18] Z. Q. Yu, S. Zhang, and H. Zhai, Stability condition of a strongly interacting boson-fermion mixture across an interspecies Feshbach resonance, *Phys. Rev. A* **83**, 041603(R) (2011).
- [19] M. Olshanii, Atomic Scattering in the Presence of an External Confinement and a Gas of Impenetrable Bosons, *Phys. Rev. Lett.* **81**, 938 (1998).

- [20] I. Fritsche, C. Baroni, E. Dobler, E. Kirilov, B. Huang, R. Grimm, G. M. Bruun, and P. Massignan, Stability and breakdown of Fermi polarons in a strongly interacting Fermi-Bose mixture, *Phys. Rev. A* **103**, 053314 (2021).
- [21] C. Mora and F. Chevy, Normal Phase of an Imbalanced Fermi Gas, *Phys. Rev. Lett.* **104**, 230402 (2010).
- [22] B. DeSalvo, K. Patel, G. Cai, and C. Cheng, Dipole Oscillations of a BEC Immersed in a Degenerate Fermi Gas, *Nature* **568**, 61 (2019).
- [23] M. Cetina, M. Jag, R. S. Lous, I. Fritsche, J. T. M. Walraven, R. Grimm, J. Levinsen, M. M. Parish, R. Schmidt, M. Knap, and E. Demler, Ultrafast many-body interferometry of impurities coupled to a Fermi sea, *Science* **354**, 96 (2016).
- [24] N. B. Jorgensen, L. Wacker, K. T. Skalmstang, M. M. Parish, J. Levinsen, R. S. Christensen, G. M. Bruun, and J. J. Arlt, Observation of Attractive and Repulsive Polarons in a Bose-Einstein Condensate, *Phys. Rev. Lett.* **117**, 055302 (2016).
- [25] M. G. Hu, M. J. Van de Graaff, D. Kedar, J. P. Corson, E. A. Cornell, and D. S. Jin, Bose Polarons in the Strongly Interacting Regime, *Phys. Rev. Lett.* **117**, 055301 (2016).
- [26] Z. Z. Yan, Y. Ni, C. Robens, and M. W. Zwierlein, Bose polarons near quantum criticality, *Science* **368**, 190 (2020).
- [27] M. Duda, X. Y. Chen, A. Schindewolf, R. Bause, J. von Milczewski, R. Schmidt, I. Bloch, and X. Y. Luo, Transition from a polaronic condensate to a degenerate Fermi gas of heteronuclear molecules, *arXiv:2111.04301v2* (2021).
- [28] W. Zwerger, *The BCS-BEC crossover and the unitary Fermi gas*, in: *Lectures Notes in Physics*, Vol. 836, Springer-Verlag, Berlin (2012).
- [29] Z. Zhang, L. Chen, K.-X. Yao, and C. Chin, Transition from an atomic to a molecular Bose-Einstein condensate, *Nature* **592**, 708 (2021).

-
- [30] J. T. Stewart, J. P. Gaebler, and D. S. Jin, Using photoemission spectroscopy to probe a strongly interacting Fermi gas, *Nature* **414**, 744 (2008).
- [31] Q. Chen and K. Levin, Probing the Spectral Function Using Momentum Resolved Radio Frequency Spectroscopy in Trapped Fermi Gases, *Phys. Rev. Lett.* **102**, 190402 (2009).
- [32] Y. Shin, C. H. Schunck, A. Schirotzek, and W. Ketterle, Tomographic rf Spectroscopy of a Trapped Fermi Gas at Unitarity, *Phys. Rev. Lett.* **99**, 090403 (2007).
- [33] R. Bause, A. Kamijo, X. Y. Chen, M. Duda, A. Schindewolf, I. Bloch, and X. Y. Luo, Efficient conversion of closed-channel dominated Feshbach molecules of $^{23}\text{Na}^{40}\text{K}$ to their absolute ground state, *Phys. Rev. A* **104**, 043321 (2021).
- [34] X. Y. Chen, M. Duda, A. Schindewolf, R. Bause, I. Bloch, and X. Y. Luo, Suppression of Unitary Three-body Loss in a Degenerate Bose–Fermi Mixture, *Phys. Rev. Lett.* **128**, 153401 (2022).
- [35] M. A. Ruderman, C. Kittel, Indirect Exchange Coupling of Nuclear Magnetic Moments by Conduction Electrons, *Phys. Rev.*, vol. 96, **1**, 99-102 (1954).
- [36] T. Kasuya, A Theory of Metallic Ferro- and Antiferromagnetism on Zener’s Model, *Progress of Theoretical Physics*, Vol. 16, **1**, 45-57 (1956).
- [37] K. Yosida, Magnetic Properties of Cu-Mn Alloys, *Phys. Rev.*, Vol. 106, **5**, 893-898 (1957).
- [38] M. Duda, X. Y. Chen, R. Bause, A. Schindewolf, I. Bloch, and X. Y. Luo, Long-lived fermionic Feshbach molecules with tunable p -wave interactions, arXiv:2202.06940v1 (2022).
- [39] A. Schindewolf, R. Bause, X. Y. Chen, M. Duda, T. Karman, I. Bloch, and X. Y. Luo, Evaporation of microwave-shielded polar molecules to quantum degeneracy, *Nature* **607**, 677 (2022).

- [40] S. Simonucci, P. Pieri, and G. C. Strinati, Broad versus narrow Fano-Feshbach resonances in the BCS-BEC crossover with trapped Fermi atom, *Europhys. Lett.* **69**, 713 (2005).
- [41] V. N. Popov, *Functional integrals and collective excitations*, Cambridge University Press, Cambridge (1987).
- [42] E. Fratini and P. Pieri, Mass imbalance effect in resonant Bose-Fermi mixtures, *Phys. Rev. A* **85**, 063618 (2012).
- [43] P. Pieri, L. Pisani, and G. C. Strinati, BCS-BEC crossover at finite temperature in the broken-symmetry phase, *Phys. Rev. B* **70**, 094508 (2004).
- [44] P. Pieri, L. Pisani, and G. C. Strinati, Comparison between a diagrammatic theory for the BCS-BEC crossover and quantum Monte Carlo results, *Phys. Rev. B* **72**, 012506 (2005).
- [45] A. L. Fetter and J. D. Walecka, *Quantum Theory of Many-Particle Systems*, McGraw Hill, New York (1971).
- [46] E. Fratini and P. Pieri, Single-particle spectral functions in the normal phase of a strongly attractive Bose-Fermi mixture, *Phys. Rev. A* **88**, 013627 (2013).
- [47] A. Guidini, G. Bertaina, E. Fratini, and P. Pieri, Bose-Fermi mixtures in the molecular limit, *Phys. Rev. A* **89**, 023634 (2014).
- [48] N. M. Hugenholtz and D. Pines, Ground-State Energy and Excitation Spectrum of a System of Interacting Bosons, *Phys. Rev.* **116**, 489 (1959).
- [49] A. Guidini, Ph.D. thesis, *Superconductivity and Superfluidity in Multicomponent Systems*, University of Camerino (2016).
- [50] H. Shi and A. Griffin, Finite-temperature excitations in a dilute Bose-condensed gas, *Phys. Rep.* **304**, 1 (1998).
- [51] J. M. Luttinger, Fermi Surface and Some Simple Equilibrium Properties of a System of Interacting Fermions, *Phys. Rev.* **116**, 1153 (1960).

- [52] A. Guidini, G. Bertaina, E. Fratini, and P. Pieri, Bose-Fermi mixtures in the molecular limit, *Phys. Rev. A* **89**, 023634 (2014).
- [53] W. H. Press, S. A. Tenkolsky, W. T. Vetterling, B. P. Flannery, *Numerical recipes in Fortran 90*, Cambridge University Press, Cambridge (1996).

Acknowledgements

I would like to express my full gratitude to Prof. Pierbiagio Pieri, who, very patiently, brought me closer to the fascinating physics of ultracold atoms and gave me all the support I needed during this work, and probably more. I also want to thank all the professors that taught me during my Bachelor's and Master's degree. Finally, I am grateful to my family and all the friends and colleagues that were able to give me the right motivation during these difficult but stimulating years.